Citation
Vo, N.H. and Pham, T.M. and Bi, K. and Hao, H. 2021. Model for analytical investigation on meta-lattice truss for low-frequency spatial wave manipulation. Wave Motion. 103: ARTN 102735.
http://doi.org/10.1016/j.wavemoti.2021.102735

Model for Analytical Investigation on Meta-lattice Truss for Low-frequency Spatial Wave Manipulation

Nhi H. Vo[1], Thong M. Pham[2], Kaiming Bi[3] and Hong Hao[4]

Abstract

This study proposes an analytically unprecedented model of a meta-lattice truss with local resonators to generate a broader low-frequency bandgap. By leveraging the mass-spring model, a new equivalent meta-unit cell considering the elastic shear springs is developed to accurately predict the performance of the meta-lattice truss in suppressing stress wave propagations. Theoretical analyses and numerical simulations are conducted to examine the effectiveness of the proposed model. Sensitivity analyses are also performed to investigate the influences of masses and spring parameters on the bandgap characteristics of the meta-lattice truss. Based on the theoretical prediction, the system transmission coefficient is utilized to examine the transmissibility effect among the resonators. A three-dimensional finite element model of meta-lattice truss is also built and its accuracy in predicting the stress wave propagations is verified against the analytical predictions. The structural responses in the time domain and time-frequency domain demonstrate the superiority of meta-lattice truss in suppression of wave transmission as compared to that predicted by the conventional counterparts.

[1] PhD Student, Center for Infrastructural Monitoring and Protection, School of Civil and Mechanical Engineering, Curtin University, Kent Street, Bentley, WA 6102, Australia. Email: hoangnhi.vo@postgrad.curtin.edu.au

[2] Senior Lecturer, Center for Infrastructural Monitoring and Protection, School of Civil and Mechanical Engineering, Curtin University, Kent Street, Bentley, WA 6102, Australia (Corresponding author). Email: thong.pham@curtin.edu.au

[3] Senior Lecturer, Center for Infrastructural Monitoring and Protection, School of Civil and Mechanical Engineering, Curtin University, Kent Street, Bentley, WA 6102, Australia. Email: Kaiming.bi@curtin.edu.au

[4] John Curtin Distinguished Professor, Center for Infrastructural Monitoring and Protection, School of Civil and Mechanical Engineering, Curtin University, Kent Street, Bentley, WA 6102, Australia (Corresponding author). Email: hong.hao@curtin.edu.au

Keywords: Metamaterials; Wave manipulation; Programmable design; Low-frequency bandgaps; Locally resonant, Meta-lattice model.

1. Introduction

In the last decade, the field of wave propagation has been revolutionized by the discovery of man-made materials that have the potential of wave manipulation functionalities beyond the limits of naturally available materials [1], [2]. These new concepts of artificial materials are labeled as metamaterials due to their rather exciting and exotic properties [3]. It is often taken into consideration that metamaterial is a material that contains artificial microstructures with unique characteristics that are not found in nature. This terminology originated from the field of electrodynamics, now has been extended to other branches of engineering disciplines such as the fields of acoustic and elastic materials [4], [5], [6]. Metamaterials demonstrate some superior dynamic characteristics owing to not only the constituent compositions of materials but also the engineered microstructure of configurations. At its early stage, researchers concentrated on the achievement of unconventional values of effective index [7], [8], [9]. However, it rapidly evolved towards the demonstration of exotic wave manipulation functionalities [10]. Previous studies of metamaterials exert various beneficial applications from its extraordinary characteristics, for example, seismic protection [11], [12], sound isolation [13], [14], vibration suppression [15], [16], and blast/impact mitigation [17], [18], [19]. Nonetheless, not until recently, the concept of metamaterials was extended to the context of manipulation of elastic waves in structural elements. Its application, however, still remains limited with even fewer examples of experimental verifications.

Based on their operating mechanisms [20], metamaterials are often classified into two categories, including non-resonant and locally-resonant types. The locally resonant metamaterials are generally made of inclusions in the form of hardcores coated with soft material layers, which are periodically (but not necessarily) distributed in a host matrix of dissimilar material [21], [22]. On the other hand, the non-resonant metamaterials are often made of hardcores only that are buried in a host matrix [23]. There are two mechanisms that can be utilized for metamaterials including Bragg scattering and localized resonance [24]. The bandgap behavior of non-resonant structures relies on the phenomena of wave diffraction and destructive interference with each other [25], i.e. depends on the Bragg scattering effect to form the bandgap. On the other hand, the bandgap in localized resonances is essentially independent of periodicity and symmetry, but governed by the natural frequency of the resonators.

The bandgap, which is the specific range of frequencies where propagation of an applied wave is stopped, is the most crucial features of metamaterials [26]. Therefore, much research effort primarily contributed to metamaterials' fundamental mechanism with an attempt to seek approaches to broaden the bandgap of metamaterials or make it tunable [27], [28], [29].To investigate the relation between the effective dynamic mass density and the oscillation frequency, Milton and Willis [30] proposed a rigorous model of metamaterials utilizing the typical motion equations for a rigid bar and Newton's second law to simulate the dynamic effective mass density as a function of the resonant frequency. The single mass-in-mass model was originally introduced by Huang and Sun [10] offering the negativity of mass property over a specific frequency range and this model was applied to lattice systems to broaden the bandgap by Liu et al. [31]. Motivated by the abovementioned studies, an analytical dual-resonator lattice model which was utilized to investigate the transient response of the meta-lattice truss structure was proposed by Liu et al. [32], hereafter referred as the conventional model, to further broaden the bandgap and improve the suppression of incident waves. Subsequently, the strategy of diatomic mimicking lattice systems [28] was also utilized to broaden the bandwidths of the meta-lattice truss. Besides, to investigate the effect of damping on asymmetric elastic-wave transmission, Alamri et al. [33] proposed and designed the dissipative diatomic acoustic lattice system possessing the bandwidth broadening effect. This study investigated the damping effect on the bandgaps of the lattice system while the influences of other parameters such as mass and stiffness, especially shear stiffness have not been investigated. The conventional analytical model with dual-resonator did not fully consider the importance of the shear stiffness between multilayers within the meta-lattice truss, i.e. the shear stiffness between the inner core and the coating. As will be demonstrated in the present study, this shear stiffness affects the bandgap in the low-frequency range. The accuracy of the model in predicting the transient response is therefore compromised if the shear stiffness is neglected in the analytical model. In particular, as will be proven later in this study through numerical simulations, stress wave caused by an excitation with a low range frequency, i.e. 300 Hz, is successfully mitigated in the numerical model, while the corresponding stress wave attenuation is not captured by the conventional analytical model. In other words, the conventional analytical model cannot accurately predict the response of the dual-resonator meta-lattice truss, particularly in the low-frequency range because of neglecting the shear stiffness between the inner core and the coating. Therefore, it is necessary to develop an analytical model that is able to more accurately predict the response of meta-lattice truss with dual-resonators. In the present study, an additional shear spring is introduced into the conventional analytical model, and the analytical results show the stress wave caused by the excitation with a frequency of 300 Hz is well attenuated as also observed in the numerical investigation, which demonstrates the accuracy of the proposed analytical model.

In brief, this research proposes an analytical model for the dual-resonator meta-lattice truss by adopting a locally resonant mechanism and taking the shear stiffness of all multilayers into consideration. The widely utilized mass-in-mass spring lattice model, with added shear spring to connect the inner resonator and the soft coating, is utilized to derive the analytical solutions. In this article, firstly, the analytical predictions of an infinite lattice truss member calculated by two models including the proposed model and the conventional one are derived and compared to demonstrate differences regarding the predicted bandgaps from these two models. Analytical results show that the proposed model predicts a wider bandgap in the low-frequency range, the same as the numerical model, which could not be accurately predicted by the conventional model. The comparisons with the numerical predictions based on a finite element analysis demonstrate the accuracy of the developed numerical model in this study. Specifically, if the shear stiffness is neglected, the analytical model may not accurately predict the actual response of the meta-lattice truss. The numerical model has shown an incident wave that is mitigated but the existing analytical model (without considering the shear stiffness) does not prohibit this incident wave from propagating through the truss. Therefore, this study incorporates the shear stiffness in the analytical derivation and the derived model yields good predictions as compared with the numerical results, demonstrating the need to consider the shear stiffness of the inner resonator in the analytical model. To investigate the influence of various parameters of the meta-lattice truss on wave propagation, a comprehensive parametric study is carried out and the influences of masses and spring stiffness on the behavior of the bandgap are examined. Finally, the superb stress wave attenuation ability of the meta-lattice truss with dual resonators is demonstrated.

2. Design of the dual-resonator lattice model

Without loss of generality, the example 3D meta-lattice truss model utilized in this investigation consists of 7 unit cells in which each cell comprises of five parts: the outer tube, 2 soft coats, and 2 resonators as shown in Fig. 1(a). The compositions and dimensions of each unit cell are presented in Figs. 1(b) and 1(c), respectively. Aluminium and lead are respectively selected for the outer tube and the resonators, and the two soft coatings are made from rubber. In the analytical model, the matrix is represented by material 1, i.e., the outer aluminium tube. Meanwhile, material 2 is modelled by two springs including the outside shear spring k_2 connecting the resonator with the outer shell and the axial spring k_1 connecting the adjacent resonators (refer to Fig. 3(b) for more details). Similarly, material 4 is modelled by the axial and shear springs connecting the internal hardcore mass and external hardcore mass, namely k_3 and k_4, respectively. The numerical analysis in the following sections indicates that the analytical model without considering k_4 does not reflect the actual response of the meta-lattice truss as observed in the numerical simulation presented in this study. Acting as resonators, material 3 and material 5 are represented by the external mass m_1 and internal mass m_2, respectively. It should be noted that this study is dedicated to investigate the dynamic performance of the elastic meta-lattice truss under the elastic stress wave. The properties of all the materials are summarized in Tables 1, 2 and 4. These material properties are also used in the numerical model in this study.

The inner mass and outer mass can be estimated by Eq. (1) where ρ_j and V_j are the material density and volume of the j^{th} material, and the length and radius of j^{th} unit are denoted by l_j and r_j, respectively.

$$m_j = \rho_j V_j = \rho_j \pi r_j^2 l_j \qquad j = 1,2 \tag{1}$$

Similarly, the spring of each stiffness can be estimated as follows

$$k_1 = \frac{E_3 A_1}{l_2}, \qquad k_2 = \frac{G_3 A_2}{l_1}, \qquad G_3 = \frac{E_3}{2(1+\nu_3)} \tag{2}$$

$$k_3 = \frac{E_3 A_3}{l_3}, \qquad k_4 = \frac{G_3 A_4}{l_4}$$

in which E and G are the Young's modulus and shear modulus of the soft material, respectively. The values of A_i (i=1,2,3,4) which are the nominal cross-sections of the distinct segments of the soft layer presented in the appendix are obtained by FEA due to the shape complexity. The detailed calculation of the spring stiffness is also presented in the appendix. Based on the material properties and dimensions, the relevant estimations of equivalent mass and stiffness are computed as m_1 = 14.2x10^{-3} kg, m_2 = 17.7x10^{-3} kg, k_1 = 424,655 N/m, k_2 = 102,531 N/m, k_3 = 280,526 N/m, and k_4=61,425 N/m.

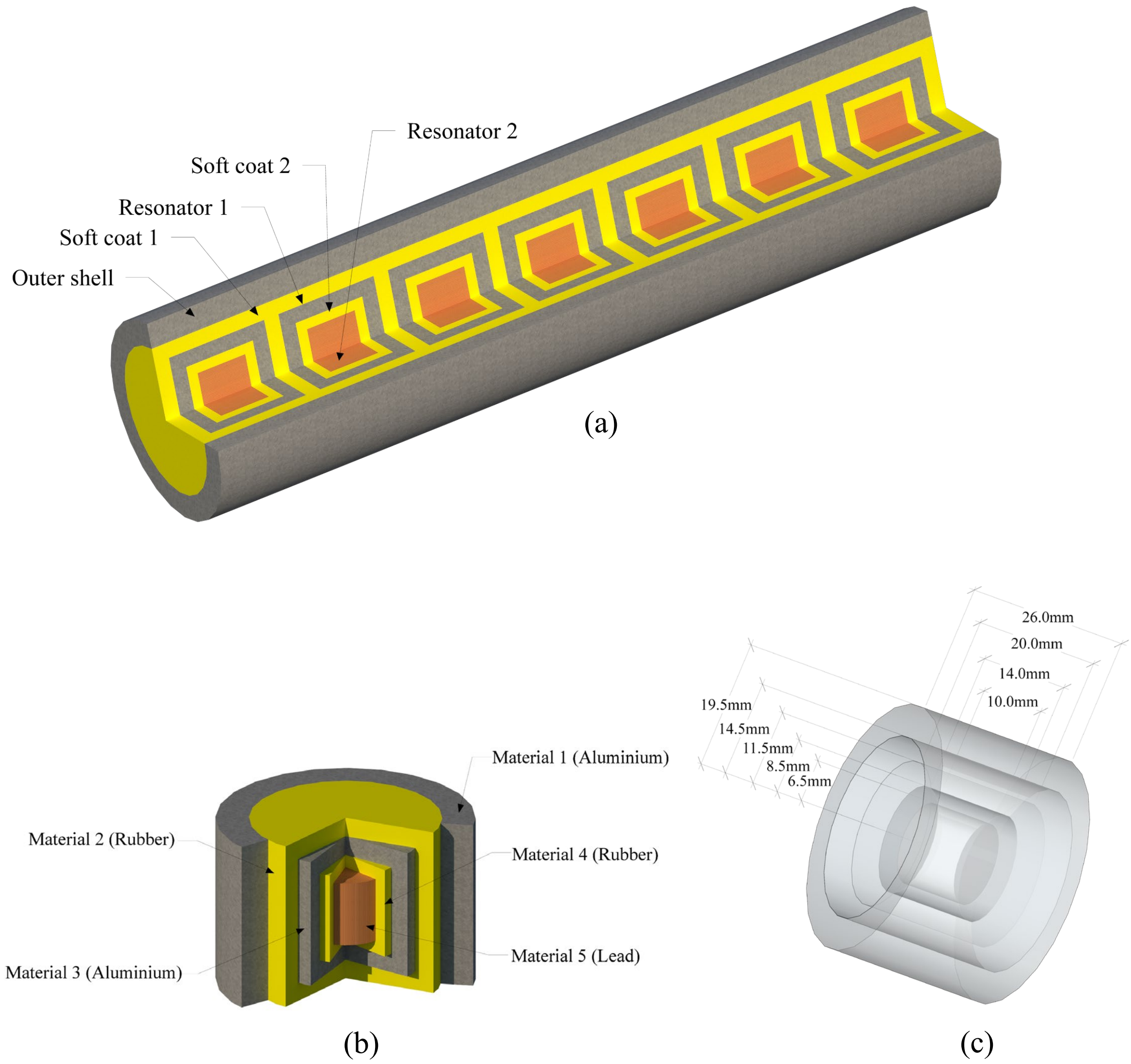

Fig. 1. (a) Schematic view of 3D lattice truss (b) Single unit cell and (c) Dimension of the single unit cell.

Table 1. Elastic material properties used in the numerical simulation [34]

Properties	Materials 1 and 3	Materials 2 and 4	Material 5
	Aluminium	Rubber	Lead
Density ρ (kg/m^3)	2770	1200	11340
Young's modulus E (Pa)	70x10^9	780x10^3	16x10^9
Poisson's ratio v	0.33	0.47	0.45

3. Analytical models

Firstly, the conventional 1D mass-spring chain model with locally resonant microstructures is briefly revisited (Section 3.1). Then, a shear spring is introduced into the unit cell, and an unprecedented model is proposed in Section 3.2. The comparisons with the conventional model in terms of transmissibility are also made in this section. Comprehensive parametric studies are further carried out in Section 5 to analytically examine the influences of mass and spring stiffness on the bandgaps.

3.1 Conventional mass-in-mass spring model of meta-lattice truss

The meta-lattice truss can be represented in the mass-in-mass formation comprising of masses and springs [32]. An infinite 1D spring-mass lattice system including the resonators is depicted in Figs. 2(a) and 2(b), in which the inner mass m_2 and outer mass m_1 are connected to each other by an axial spring k_3. The shear spring with the stiffness k_2 constrains the displacement of the mass m_1 which is periodically linked with each other by the axial spring k_1.

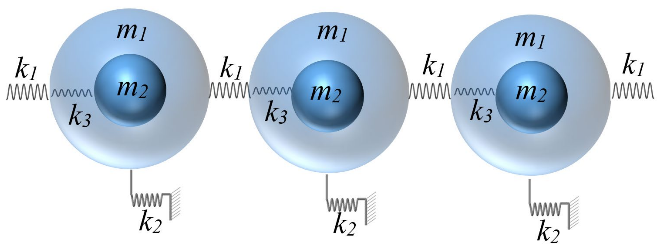

(a)

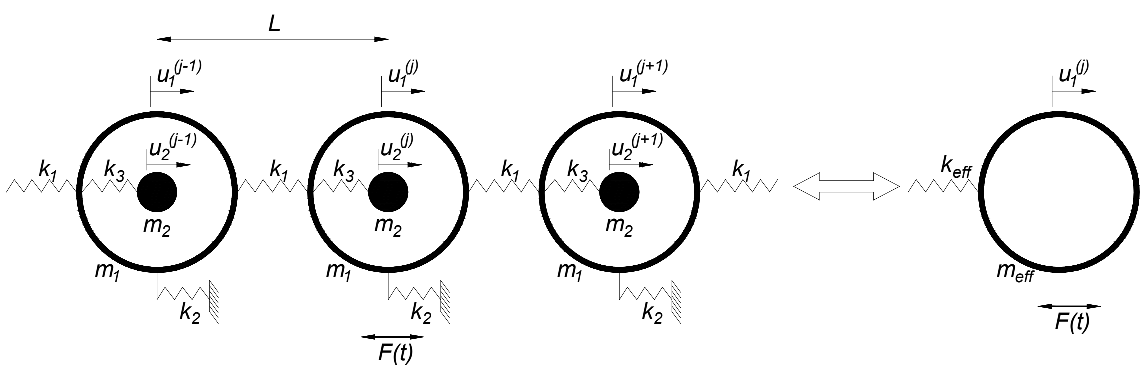

(b)

Fig. 2. (a) Schematic microstructure of the infinite conventional model of meta-lattice truss and (b) Equivalent effective spring-mass model.

In this one-dimensional meta-lattice truss, the internal and external mass displacements are denoted by u_1 and u_2, respectively, and the motion equations of the j^{th} unit cell can be derived as follows:

$$m_1\ddot{u}_1^{(j)} + k_1\left(2u_1^{(j)} - u_1^{(j+1)} - u_1^{(j-1)}\right) + k_3\left(u_1^{(j)} - u_2^{(j)}\right) + k_2 u_1^{(j)} = 0 \tag{3}$$

$$m_2\ddot{u}_2^{(j)} + k_3\left(u_2^{(j)} - u_1^{(j)}\right) = 0 \tag{4}$$

Based on the Floquet-Bloch theorem [35], the solution of harmonic wave of the *(j+n)*$^{\text{th}}$ and j^{th} unit cells can be expressed in the form of

$$u^{(j+n)} = Ue^{i(jqL+nqL-\omega t)} \tag{5}$$

$$u^{(j)} = Ue^{i(jqL-\omega t)} \tag{6}$$

where U is the displacement amplitude, q is the wavenumber, ω is the angular frequency, L is the length of the unit cell.

By substituting Eqs. (5) and (6) into Eqs. (3) and (4), the dispersion relation of the lattice system can be derived as follows:

$$\cos qL = 1 - \frac{m_1\omega^2 - \left(k_2 + k_3\right) + \dfrac{k_3^2}{k_3 - m_2\omega^2}}{2k_1} \tag{7}$$

Herein, the lattice system is monatomic, therefore, the following effective mass equation of the microstructure must be satisfied

$$\omega^2 = 2\frac{k_1}{m_{eff}}\left(1-\cos qL\right) \tag{8}$$

Based on Eqs. (7) and (8), the effective mass (m_{eff}) of the lattice system can be obtained as:

$$m_{eff} = m_1 - \frac{k_2+k_3}{\omega^2} + \frac{k_3^2}{k_3\omega^2 - m_2\omega^4} \tag{9}$$

When the unit cell is regarded as homogeneous with the effective mass m_{eff} and effective stiffness k_{eff} (Fig. 2(b)), the effective stiffness can be calculated as follows [32]:

$$k_{eff} = k_1 - \frac{1}{4}m_{eff}\omega^2 = k_1 + \frac{1}{4}\left(k_2+k_3\right) - \frac{1}{4}\left(m_1\omega^2 + \frac{k_3^2}{k_3 - m_2\omega^2}\right) \tag{10}$$

To define the width of the bandgap, the dispersion in Eq. (7) can be solved and the expression of the angular frequency can be obtained as follows:

$$\omega^2 = \frac{m_2k_2 + \left(m_1+m_2\right)k_3 + 2k_1m_2\left(1-\cos qL\right) \pm \sqrt{\beta}}{2m_1m_2} \tag{11}$$

where $\beta = \left(m_2k_2 + \left(m_1+m_2\right)k_3 + 2k_1m_2\left(1-\cos qL\right)\right)^2 - 4m_1m_2\left[2k_1k_3\left(1-\cos qL\right) + k_2k_3\right]$

Substituting qL=0, the angular frequency at the starting points of two passbands can be obtained as:

$$\omega^2 = \frac{m_2k_2 + \left(m_1+m_2\right)k_3 \pm \sqrt{m_2^2k_2^2 + \left(m_1+m_2\right)^2 k_3^2 + 2k_2k_3\left(m_2^2 - m_1m_2\right)}}{2m_1m_2} \tag{12}$$

and substituting qL=π, the angular frequency at the two ending points of the passband can be expressed as:

$$\omega^2 = \frac{\left(m_1+m_2\right)k_3 + 4m_2\left(k_1+k_2\right) \pm \sqrt{\left(m_2k_2 + \left(m_1+m_2\right)k_3 + 4k_1m_2\right)^2 - 4m_1m_2\left[4k_1k_3 + k_2k_3\right]}}{2m_1m_2} \tag{13}$$

3.2 Proposed mass-in-mass spring model of meta-lattice truss

As shown in Fig. 2 and also discussed in the introduction, the conventional meta-lattice model proposed by Liu, Shen, Su and Sun [32] only considered the shear spring connected the external mass m_1 and the soft layer (material 2 in Fig. 1), and it is represented by k_2. The shear spring linking the internal mass m_2 and the corresponding soft layer (material 4 in Fig. 1) was, however, neglected. It is obvious that the inner mass and the outer mass of a unit cell bear similar characteristics, and the negligence of this stiffness may result in inaccurate bandgap predictions. It is therefore worth considering the shear stiffness of the inner mass to enhance the accuracy of the model. This study proposes an improved mass-in-mass spring meta-lattice model, in which besides the spring with the stiffness k_2 constrains the displacement of the mass m_1 to the matrix, the inner mass m_2 is also restrained by the shear spring stiffness k_4. Figs. 3(a) and 3(b) show the corresponding analytical model.

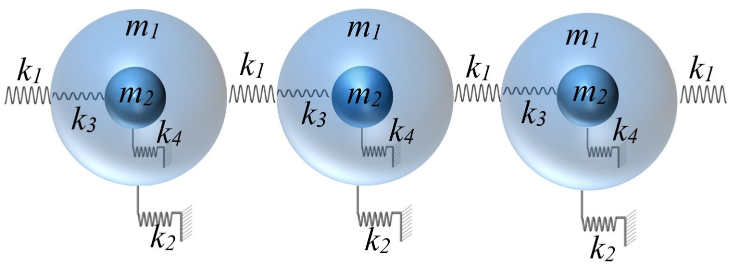

(a)

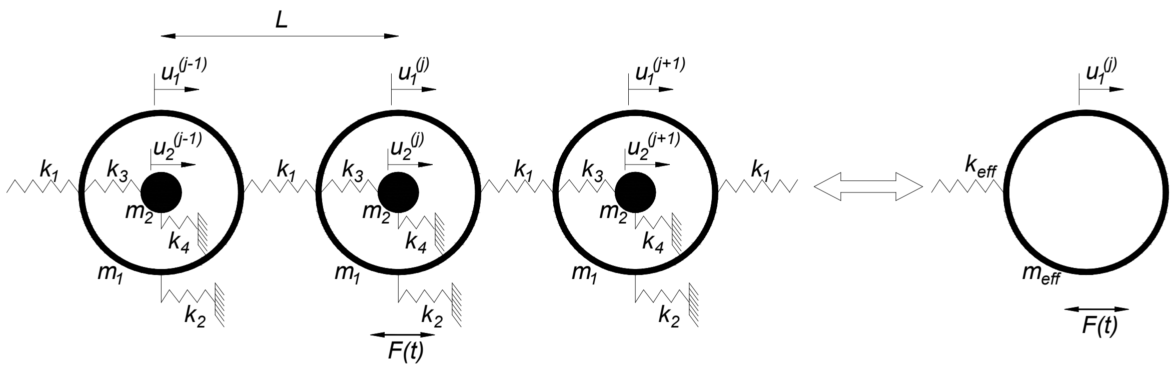

(b)

Fig. 3. (a) Schematic microstructure of the proposed model of meta-lattice truss and (b) Equivalent effective mass-spring model.

Similar to the conventional mass-in-mass spring model as shown in Fig. 2, the equations of motion of the j^{th} unit cell in Fig. 3 can be expressed as follows:

$$m_1\ddot{u}_1^{(j)}+k_1\left(2u_1^{(j)}-u_1^{(j+1)}-u_1^{(j-1)}\right)+k_3\left(u_1^{(j)}-u_2^{(j)}\right)+k_2u_1^{(j)}=0 \tag{14}$$

$$m_2\ddot{u}_2^{(j)}+k_3\left(u_2^{(j)}-u_1^{(j)}\right)+k_4u_2^{(j)}=0 \tag{15}$$

To derive the dispersion curves, a similar strategy is adopted and the solution of harmonic wave of the $(j+n)^{\mathrm{th}}$ and j^{th} unit cells can be represented by Eq. (5) again, and the derivative function of the solution can be obtained as follows

$$\ddot{u}^{(j)}=-\omega^2Ue^{i(jqL-\omega t)}=-\omega^2u^{(j)} \tag{16}$$

Substituting Eq. (16) into Eq. (15), the relation between the inner mass and outer mass can be obtained as follows:

$$u_2^{(j)}=\frac{k_3}{k_3+k_4-m_2\omega^2}u_1^{(j)} \tag{17}$$

It is worth noting that the Bloch-Floquet theory consequence is adopted in the present study, in which the motion must satisfy the Bloch periodicity condition. Hence, by substituting Eqs. (16) and (17) into Eq. (14), one obtains

$$-m_1\omega^2u_1^{(j)}+k_1\left(2u_1^{(j)}-u_1^{(j)}e^{-iqL}-u_1^{(j)}e^{iqL}\right)+k_3\left(1-\frac{k_3}{k_3+k_4-m_2\omega^2}\right)u_1^{(j)}+k_2u_1^{(j)}=0 \tag{18}$$

By applying the identity $e^{-iqL}+e^{iqL}=2\cos\left(qL\right)$, Eq. (18) can be rewritten to form the dispersion relation as follows:

$$\cos qL = 1 - \frac{m_1\omega^2 - \left(k_2 + k_3\right) + \dfrac{k_3^2}{\left(k_3 + k_4\right) - m_2\omega^2}}{2k_1} \tag{19}$$

Eq. (19) can also be rearranged into the following form

$$\omega^2 = 2\frac{k_1}{m_{eff}}\left(1 - \cos qL\right) \tag{20}$$

where

$$m_{eff} = m_1 - \frac{k_2 + k_3}{\omega^2} + \frac{k_3^2}{\left(k_3 + k_4\right)\omega^2 - m_2\omega^4} \tag{21}$$

and the effective stiffness can also be conveniently formulated due to the homogeneity of the unit cell

$$k_{eff} = k_1 + \frac{1}{4}\left(k_2 + k_3\right) - \frac{1}{4}\left(m_1\omega^2 + \frac{k_3^2}{\left(k_3 + k_4\right) - m_2\omega^2}\right) \tag{22}$$

With an attempt to find the dispersion relation for this system, the angular frequency can be calculated by solving Eq. (19) as follows:

$$\omega^2 = \frac{2m_2\left(1 - \cos qL\right)k_1 + m_2k_2 + \left(m_1 + m_2\right)k_3 + m_1k_4 \pm \sqrt{\gamma - \eta}}{2m_1m_2} \tag{23}$$

where $\gamma = \left(2m_2\left(1 - \cos qL\right)k_1 + m_2k_2 + \left(m_1 + m_2\right)k_3 + m_1k_4\right)^2$ and $\eta = 4m_1m_2\left[2k_1\left(k_3 + k_4\right)\left(1 - \cos qL\right) + k_2\left(k_3 + k_4\right) + k_3k_4\right]$.

The above derivations are based on the assumption of infinite unit cell. In practice, the number of unit cells is always finite. In this case, the wave transmission coefficient of the spring-mass chain, which depicts the displacement amplitude ratio of the last unit cell to the input excitation is normally defined, and it can be calculated as follows Yao et al. [36]:

$$T = \left| \prod_{j=1}^{N} T^{(j)} \right| \tag{24}$$

where $T^{(j)} = u^{(j)} / u^{(j-1)}$

From Eq. (20), by applying the identities $e^{-iqL} + e^{iqL} = 2\cos(qL)$ and rearranging the equation the following form can be obtained:

$$\left(2k_1 - \omega^2 m_{eff}\right) u^{(j)} = k_1 \left(u^{(j+1)} + u^{(j-1)}\right), \quad j = 1, 2, ..., N-1 \tag{25}$$

$$\left(k_1 - \omega^2 m_{eff}\right) u^{(j)} = k_1 u^{(j-1)}, \quad j = N \tag{26}$$

Substituting $T^{(j)} = u^{(j)} / u^{(j-1)}$ into Eqs. (25) and (26) gives:

$$2k_1 - \omega^2 m_{eff} = k_1 \left(T^{(j+1)} + \frac{1}{T^{(j)}} \right) \tag{27}$$

Therefore, the wave transmission coefficient can be formulated as follows:

$$T^{(j)} = \frac{k_1}{k_1 \left(2 - T^{(j+1)}\right) - \omega^2 m_{eff}}, \quad j = 1, 2, ..., N-1 \tag{28}$$

$$T^{(N)} = \frac{k_1}{k_1 - \omega^2 m_{eff}}, \quad j = N \tag{29}$$

4. Numerical simulation

To verify the accuracy of the proposed and conventional analytical models, a 3-D finite element model of the meta-lattice truss is built and validated in this section.

4.1 Numerical model development

The 3-D numerical model is built to investigate the wave transmission characteristics of the meta-lattice truss and verify its accuracy against the analytical predictions by utilizing commercial software LS-DYNA (Fig. (1)). Contact definitions, the prevention of reflected waves, material models, and simulation of prescribed displacement are presented in this section. In this study, all elements are modelled by solid elements and the minimum meshing size is 0.2mm after a convergence test. To define the property of aluminium considering the plastic deformation, *MAT_JOHNSON_COOK is utilized while *MAT_ELASTIC material model is applied to simulate the dynamic behaviour of rubber elements due to their distinguished properties [34]. Johnson-cook material model requires an equation of state in order to initialize the thermodynamic state of the material [37]. The elastic and plastic material properties are summarized in Tables 1 and 2, respectively. In this study, the equation of state of Johnson-cook model is defined by the card *EOS_LINEAR_POLYNOMINAL in which the pressure and initial relative volume are denoted by coefficients C_0-C_6 and V_0, respectively. The parameters for the equation of state are presented in Table 3. Furthermore, for simulation of the lead core, the material properties as implemented in *MAT_PLASTIC_KINEMATIC, are given in Table 4 [38]. The contact between the metals and rubber is modelled by the keyword *TIED_SURFACE_TO_SURFACE and the keyword *CONTACT_INTERIOR is utilized for the rubber to eliminate the negative volume issue which often occurs due to large deformation of soft materials. Additionally, to eliminate the stress wave reflection at the end surface, the keyword *NON_REFLECTING_BOUNDARY is applied at one end. In the numerical model, the far-end of the outer tube is fixed in all directions while the excitation is defined by the *PRESCRIBED_MOTION_SET card, which is applied to the entire near-end surface.

Table 2. Johnson-cook material parameters for aluminium [34]

Density (kg/m^3)	Poisson's ratio	Young's Modulus (GPa)	A (Pa)	B (Pa)	C	m	n	T_m	$\dot{\varepsilon}_0$ (1/s)
2770	0.33	70	0.369	0.675	0.007	1.5	0.7	800	1.0

Table 3. Equation of state for aluminium used in the numerical simulation [37]

C_0 (Pa)	C_1 (Pa)	C_2 (Pa)	C_3 (Pa)	C_4	C_5	C_6	E_0 (Pa)	V_0 (m^3/m^3)
0	$74.2x10^9$	$60.5x10^9$	$36.5x10^9$	1.96	0	0	0	1

Table 4. Plastic kinematic material parameters for lead [38]

Density (kg/m^3)	Poisson's ratio	Young's Modulus (GPa)	SIGY (MPa)	ETAN (MPa)	BETA	SRC	SRP	FS	VP (1/s)
11340	0.45	16	20	50	10^9	10^9	1	0	1

4.2 Numerical model verification

Based on the Bloch-Floquet theory and the derivation from Eq. (28), a visible manifestation of the theoretical transmittance of the proposed model is shown in Fig. 4. To verify the model, the meta-lattice truss comprising of 7 unit cells described above is built in LS-DYNA. The model is used to simulate wave transmissions of the meta-lattice truss. The transmittance is defined by a ratio between the output and the input signals of the structure. Fig. 4 shows the results from the conventional model, the proposed model, and the numerical simulation. It can be seen that both conventional and the proposed models capture three bandgaps, and the corresponding ranges are: [0-289.5], [645-995] and [1945-5000] Hz from the conventional model, and [0-375] Hz, [700-1100] Hz and [1945-5000] Hz from the proposed model. The numerical simulation also gives three bandgaps in the range of [0-375] Hz, [895-1400] Hz and [1965-5000] Hz. These results indicate that, generally speaking, both the conventional and the proposed model can predict the frequency bandgaps, but compared with the results from the numerical simulations, the proposed model yields more accurate results than the conventional model, especially for the 1st bandgap in the low-frequency range. For example, the proposed model predicts the same 1st bandgap as compared to the numerical model, whereas the conventional model substantially under predicts the upper frequency of the first bandgap, i.e., 289.5 Hz and 375 Hz, i.e., a substantially narrower first bandgap by the conventional model. These results demonstrate that neglecting the stiffness k_4 into the conventional analytical model leads to inaccurate predictions of the bandgap width at the low-frequency range. The comparison also shows that certain discrepancy exists between the analytical and numerical predictions, especially for the second bandgap. This is because the theoretical results are based on the infinite number of unit cells, while the numerical results are obtained from the finite number of cells (7 in the present study). Moreover, the estimations of the spring stiffness and lumped masses in the analytical derivations may also contribute to this variation.

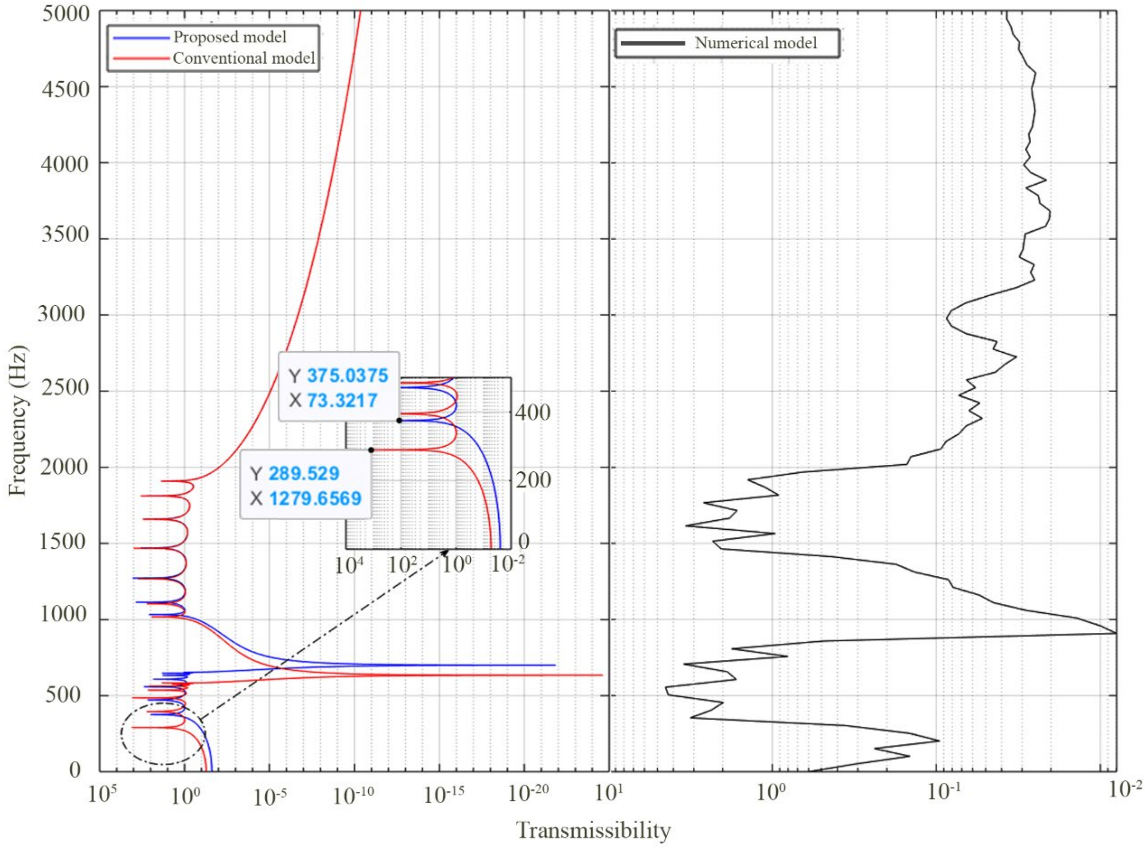

Fig. 4. Transmittance profiles of meta-lattice truss obtained by the proposed model, conventional model, and numerical simulation model.

4.3 Accuracy of the proposed analytical model

The above results show that the inclusion of k_4 in the proposed model has almost no influence on the third bandgap because the third bandgaps is mainly controlled by the external mass and axial stiffness which will be discussed in the following section. For the second bandgap, the lower bound of the proposed model results in a slightly higher value, while its influence on the upper bound is negligible. The most evident effect of the proposed model is on the first bandgap, and the inclusion of k_4 obviously widens the bandgap in the low-frequency range. As shown, the first bandgap expends from [0-289.5] Hz to [0-375.0] Hz. This result is expected, since the first bandgap is related to the local resonance frequency of the inner mass m_2 which is defined by $\varpi = \sqrt{(k_3 + k_4) / m_2}$, and the inclusion of k_4 results in an increase in the stiffness in the conventional model. Moreover, the bandwidth of the first bandgap in the low-frequency range is determined by two points including the constant value at zero and a certain value which is linearly dependent on the local resonance frequency. Therefore, introducing the shear stiffness of the internal mass k_4 increases the stiffness of the internal coating layer and resonant frequncy ω accordingly, which leads to the increase of the first bandgap range by the reciprocal relationship between the first bandgap and the resonant frequency. This manifestation indicates that the proposed analytical model with considering the shear stiffness of the soft coating leads to a wider bandgap estimation in the low-frequency range than the conventional model, which implies the proposed analytical model would have wider practical applications for stopping the low-frequency wave propagations. It is worth mentioning that, besides varying the stiffness, the low-frequency bandgap can also be changed by altering the resonator's geometry since it is related to the local resonance as discussed above, and will be further discussed in the following investigations.

To further demonstrate the higher accuracy of the proposed analytical model in predicting the bandgap in the low-frequency range compared to the conventional model, the analytically predicted bandgap are compared with the result from the numerical analyses. As discussed above, the inclusion of k_4 most evidently changes the bandgap in the low-frequency range, therefore only the first bandgap is investigated in this section. For the other two bandgaps, more detailed discussions will be given in Section 5. However, it is worth noting that the soft material layer (material 4 in Fig. 1) is modelled by the solid elements in the numerical simulation, which means the contribution from the shear stiffness of this layer (i.e. k_4) is considered in the numerical model.

In the numerical simulation, the meta-lattice truss presented in Section 2 is subjected to a displacement time history with two frequency components $u(t)=10^{-4}[\sin(2\pi f_1 t) + \sin(2\pi f_2 t)]$, where f_1=300 Hz and f_2=500 Hz. Fig. 5(a) shows the displacement time history of the excitation at the left end of the truss. It can be seen that f_1 is deliberately desinged to fall within the first bandgap of the proposed model but beyond that of the conventional model, while f_2 is within the passband range of both the models. Fig. 5(b) shows the displacement time history at the right end of the meta-lattice truss (i.e. the output) obtained from the numerical simulation, and Fig. 6 shows the Fourier spectrum of the output data. The numerical results have shown that only one input signal with the frequency of 500 Hz passes through the meta-lattice truss while the conventional model predicts both input signals pass through the structure. This observation shows that the predictions of the conventional model and numerical model are different. Meanwhile, the proposed model predicts only the signal with the frequency of 500 Hz can pass the meta-lattice truss while the other one with the frequency of 300 Hz is filtered out, which matches well with the numerical results. This results demonstrates again that neglecting the shear stiffness k_4 in the conventional model leads to inaccurate estimation of the bandgap width in the low-frequency range.

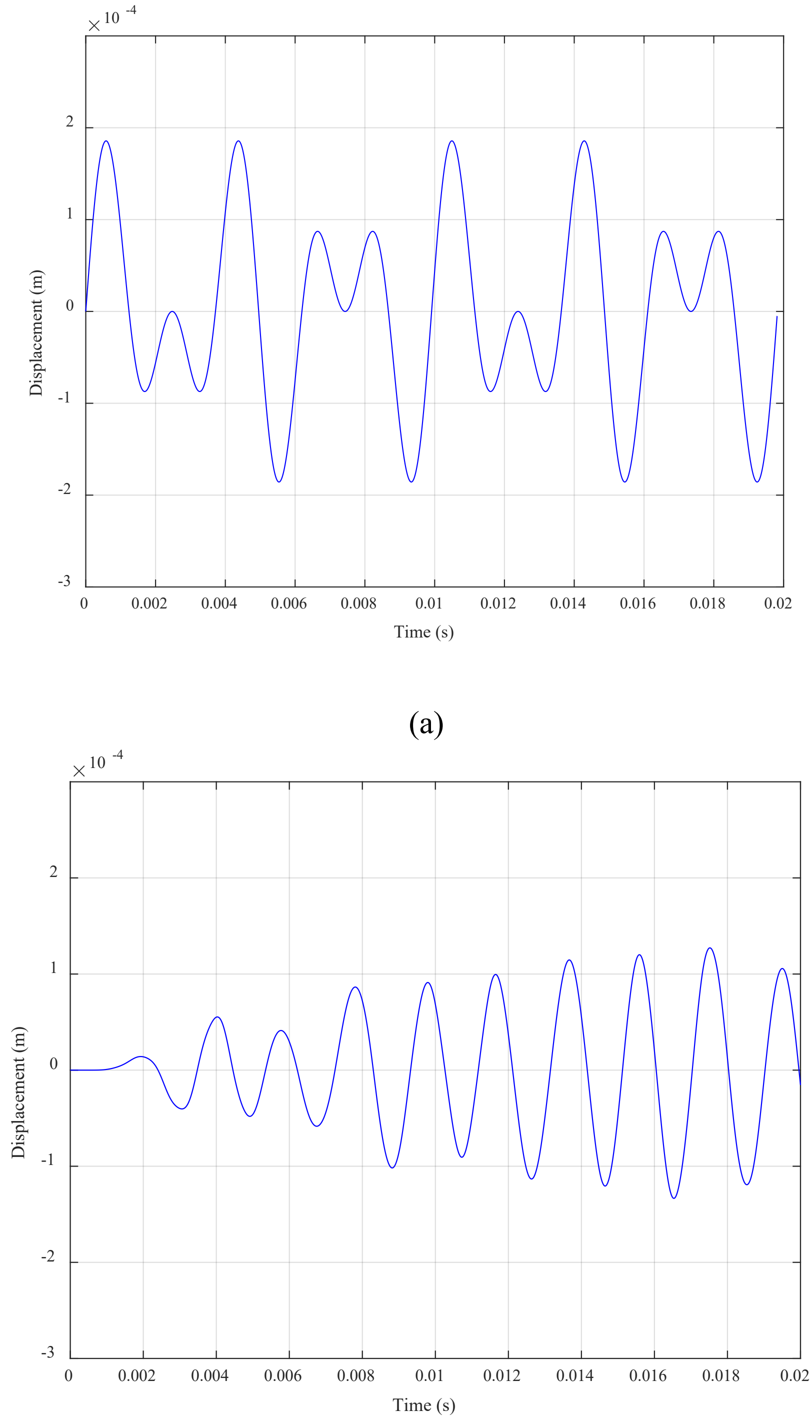

(a)

(b)

Fig. 5. Displacement time history of meta-lattice truss in numerical simulation (a) Input, (b) Output.

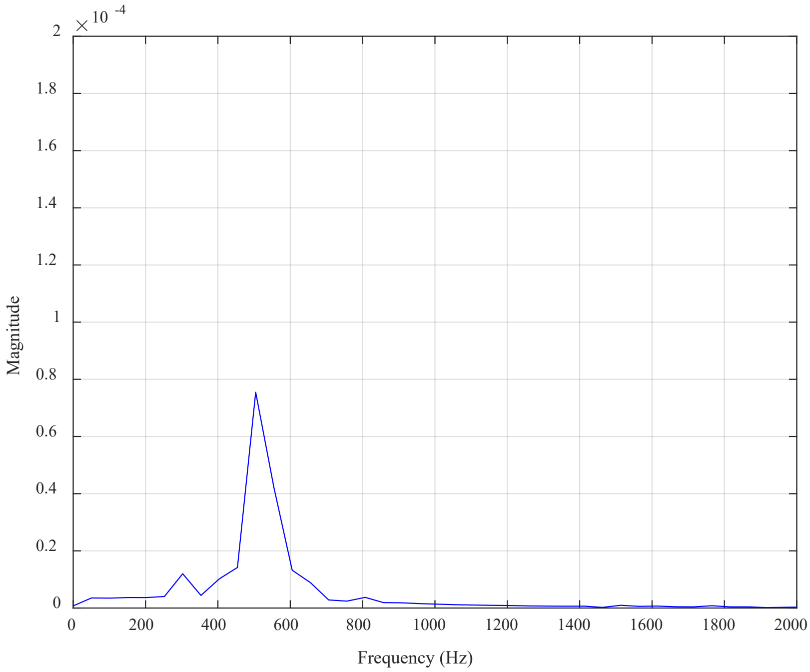

Fig. 6. The Fourier spectrum of the output data at the right end of the truss of the numerical model.

5. Sensitivity of the bandgap characteristics to mass and stiffness based on the proposed analytical model

The accuracy of the proposed analytical model has been verified against the numerical simulation and thus it is utilized to investigate the mitigation effects of the meta-lattice truss. It is worth mentioning that the sensitivity analysis of those parameters has not been presented in the literature yet.

5.1 Effect of mass on bandwidth and bandgap position

Herein, the attenuation effect of mass including the inner and outer masses on the overall bandwidth of the meta-lattice model is investigated utilizing the proposed analytical model. Based on the Bloch-Floquet theorem, the analytical dispersion curves for the lattice model are obtained and featured in Fig. 7 through the theoretical calculation of Eq. (19). It should be noted that to calculate the theoretical starting and ending frequencies of the passbands the conditions qL= 0 and qL=π are applied to Eq. (23). It can be seen that there is an unequivocal manifestation from the figure showing that there are two passbands including the first passband at the frequency range of approximately 375–700 Hz and the second passband at a relatively higher frequency range of 1000–1945 Hz.

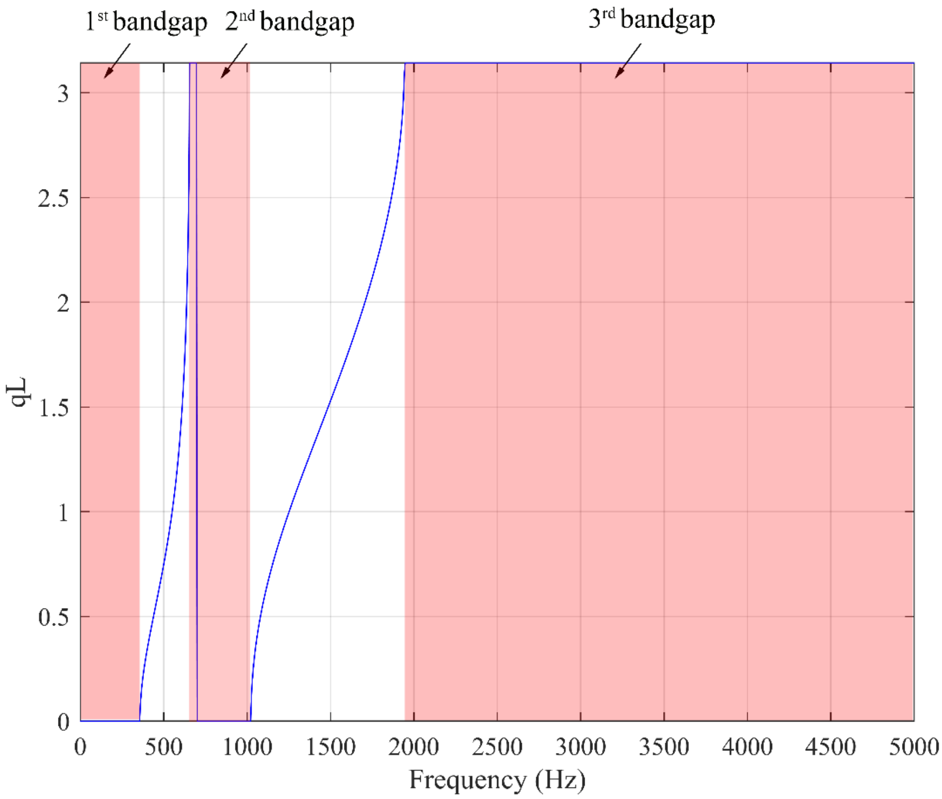

Fig. 7. Non-dimensionalized dispersion curves obtained by the proposed analytical model.

The bandgap behavior of meta-lattice truss is affected remarkably by the peculiar nature of local resonators consisting of the internal mass and external mass. Therefore, it is pivotal to examine the influence of the resonator on the meta-lattice truss bandgap with respect to critical masses by utilizing the proposed model. Figs. 8(a) and 8(b) show the two integral features of the locally resonant meta-lattice truss, i.e. the effective mass and the effective stiffness, by varying the internal mass m_2 (0.5α, α and 2α, where α= m_2). It is obvious that the bandwidth and the position of the first two bandgaps (Fig. 8(a)) associated with lower frequency are affected by the mass m_2 while the third bandgap (Fig. 8(b)) with higher frequency resulting from the stiffness remains unchanged. The analytical results also indicate that the inextricable relationship between the position of the bandgap and the local resonance frequency is a function of m_2. Fig. 8(a) clearly exhibits that the location of the first two bandgaps drastically shifts to the left with an increase of the internal mass. On the contrary, it is clear that the negativity of effective stiffness which forms the third bandwidth shown in Fig. 8(b) remains unchanged, irrespective of the changing value of m_2.

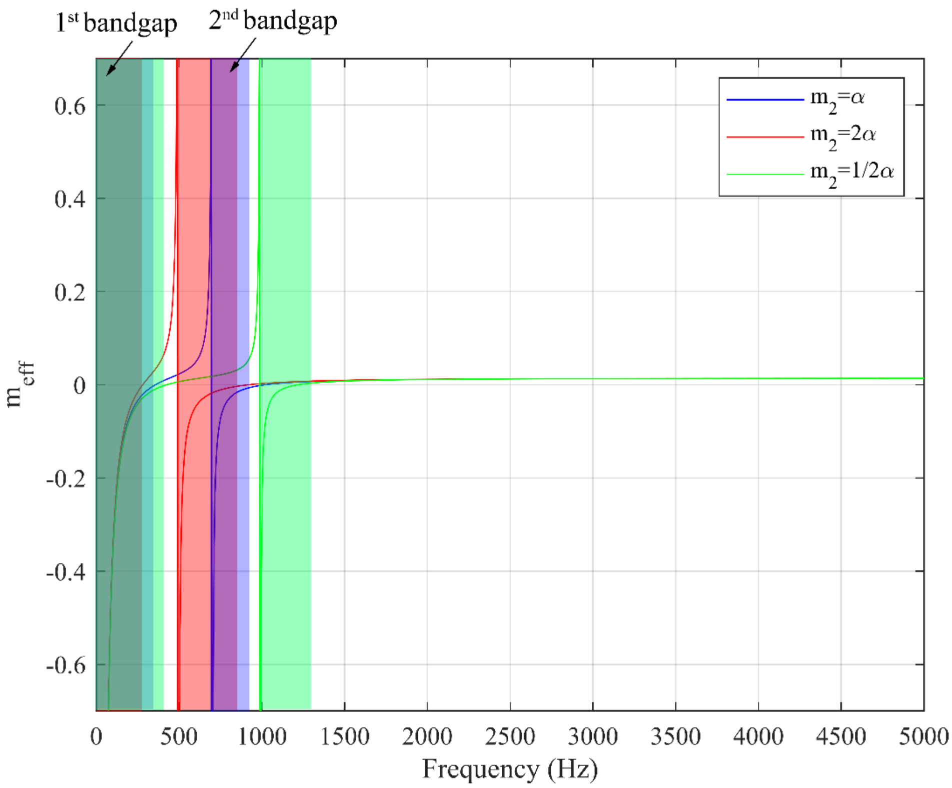

(a) Effective mass

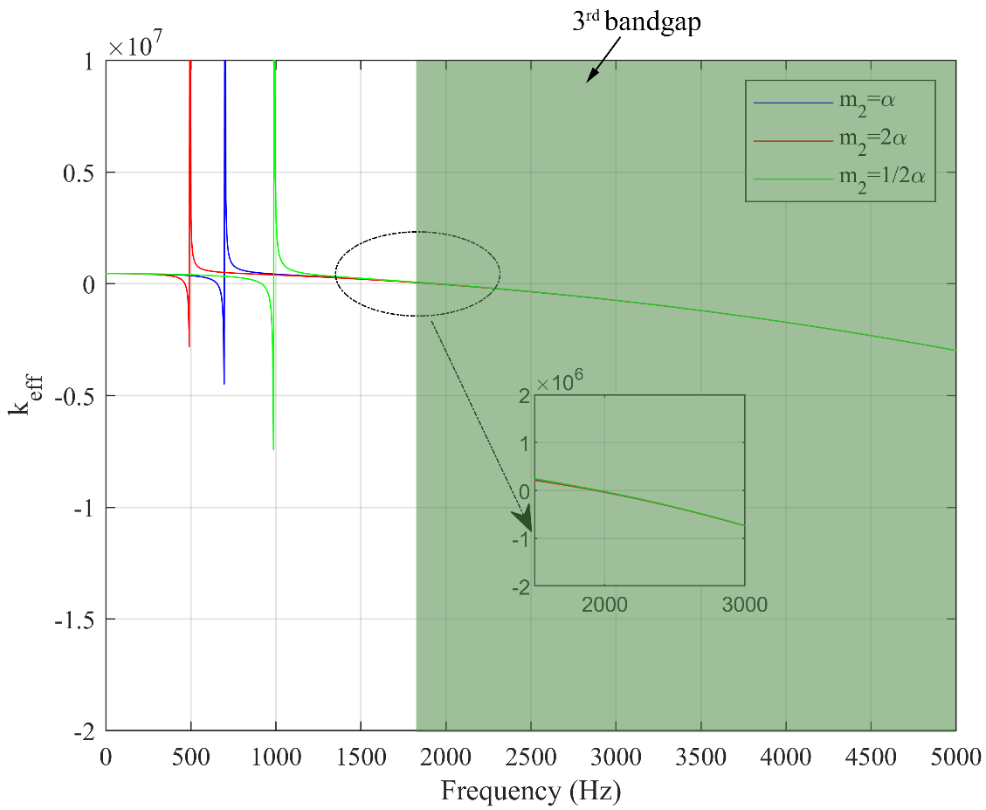

(b) Effective stiffness

Fig. 8. Effect of the internal mass m_2 on the bandgap characteristics.

Figs. 9(a) and 9(b) show the influence of the outer mass m_1 on the effective mass and stiffness, respectively. The other parameters are exactly the same as those in Table 5. Primarily, the bandgap position which is determined by the local resonance frequency has not exerted any effects by varying the value of m_1. An increase of m_1 results in a reduction in the first and second bandwidths in which the effective mass becomes negative as shown in Fig. 9(a) but increase significantly the third bandwidth which results from the negativity of the effective stiffness (Fig. 9(b)). In general, the negativity of the effective mass and effective stiffness relates to the bandgap region of the system in terms of wave propagation.

The above analytical results clearly indicate that the bandgaps could be controlled by varying the values of the internal mass m_2 and external mass m_1 to achieve the desired optimal wave manipulation. Moreover, the outer mass m_1 is more sensitive to the third bandgap associated with higher frequency while the inner mass m_2 shows a more significant influence on the first and second bandgaps which are located in a lower-frequency region. It is noted that the sensitivity can be qualitatively predicted by analyzing the relationship between m_1 and m_2 with m_{eff} and k_{eff} in Eqs. (21) and (22), considering that m_{eff} is related to the first and second bandgaps while k_{eff} governs the third bandgap. As shown in Figs. 8 and 9, in which the value of m_1 is varied 10 times while that of m_2 is only varied 2 times to show the variation in the bandgap characteristic. This observation indicates that the internal mass which significantly influences the local resonance frequency of the meta-lattice truss is more sensitive, compared to the external mass, in terms of the bandgap characteristics in wave propagation.

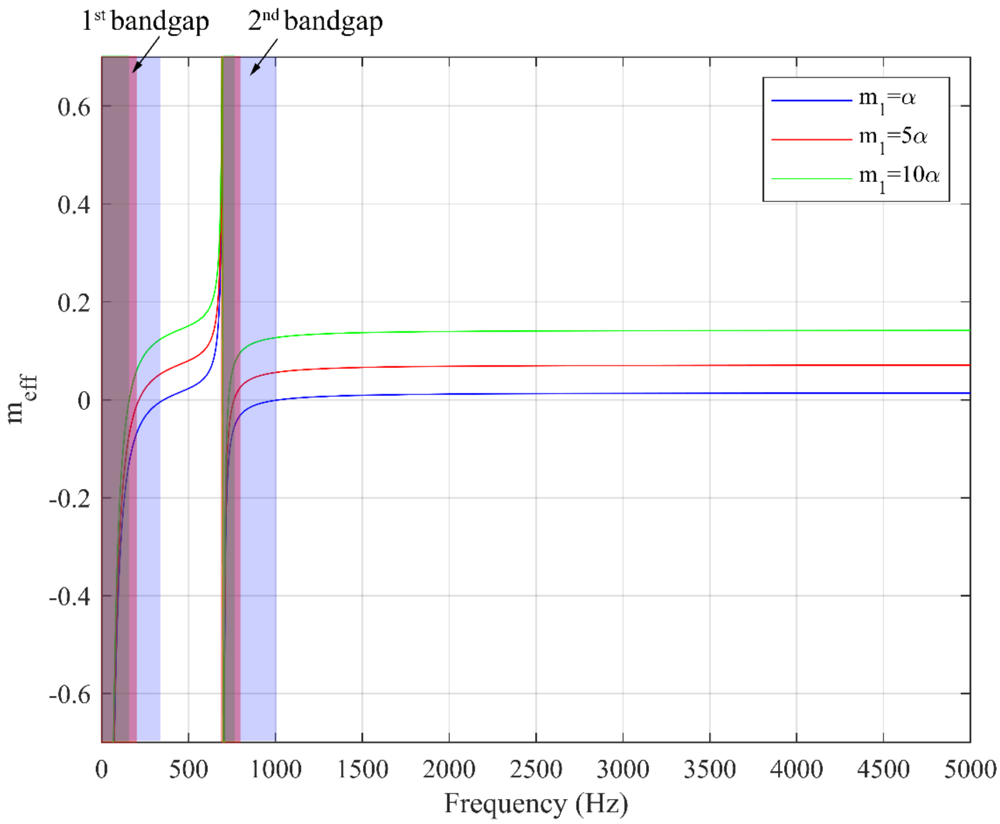

(a) Effective mass

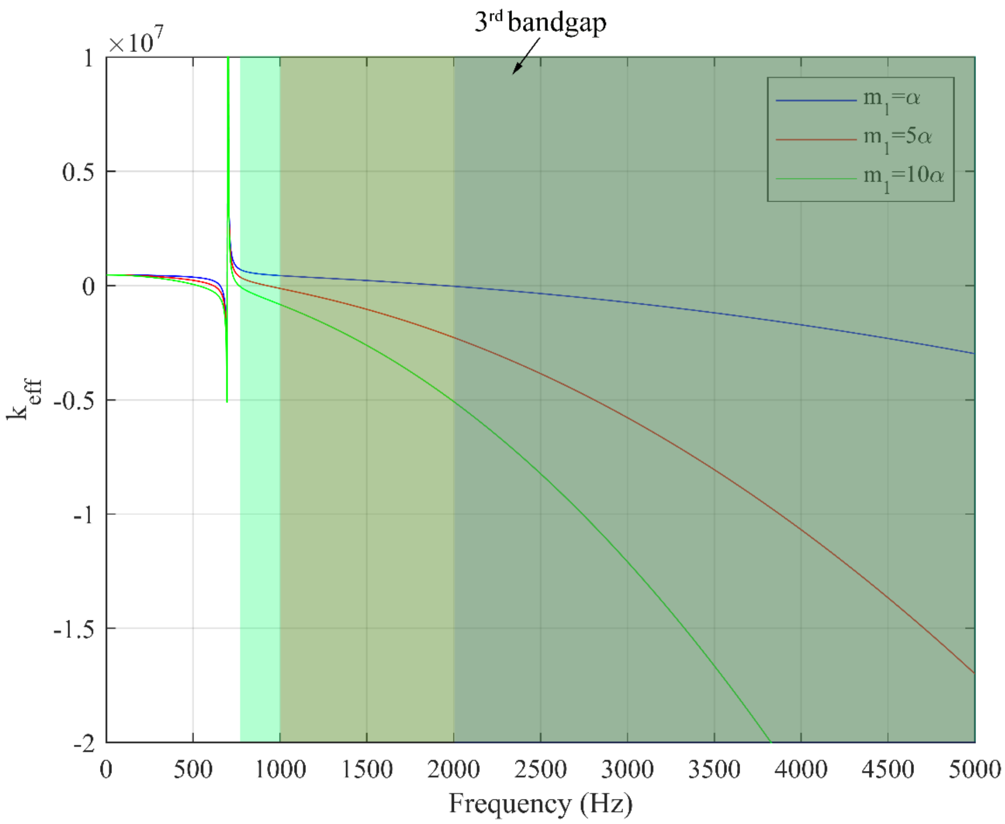

(b) Effective stiffness

Fig. 9. Effect of the internal mass m_1 on the bandgap characteristics.

5.2 Effect of spring stiffness on the bandwidth and bandgap position

The proposed model includes the additional parameter k_4 which represents the shear stiffness of the inner core while the other factors that affect the bandgap k_1, k_2, and k_3 remain the same. The effect of the stiffness k_4 on the bandwidth and the bandgap position is investigated in this section. Fig. 10 illustrates the typical wave dispersion relations of the lattice system with respect to different values of k_4. From Fig. 10, the following three primary findings can be summarized: (1) the internal resonance frequency is affected considerably due to the contribution of the stiffness k_4; (2) dissimilar to the conventional model, the characteristic of the bandgap generated by the proposed model has a wider frequency bandgap at low-frequency range, for instance, the upper bound of the first bandgap increases from 375 Hz to 655 Hz by varying k_4 from α to 10α;

and (3) the bandgap in the high frequency range mostly formed by the negativity of the effective stiffness remains unchanged regardless of the varying k_4.

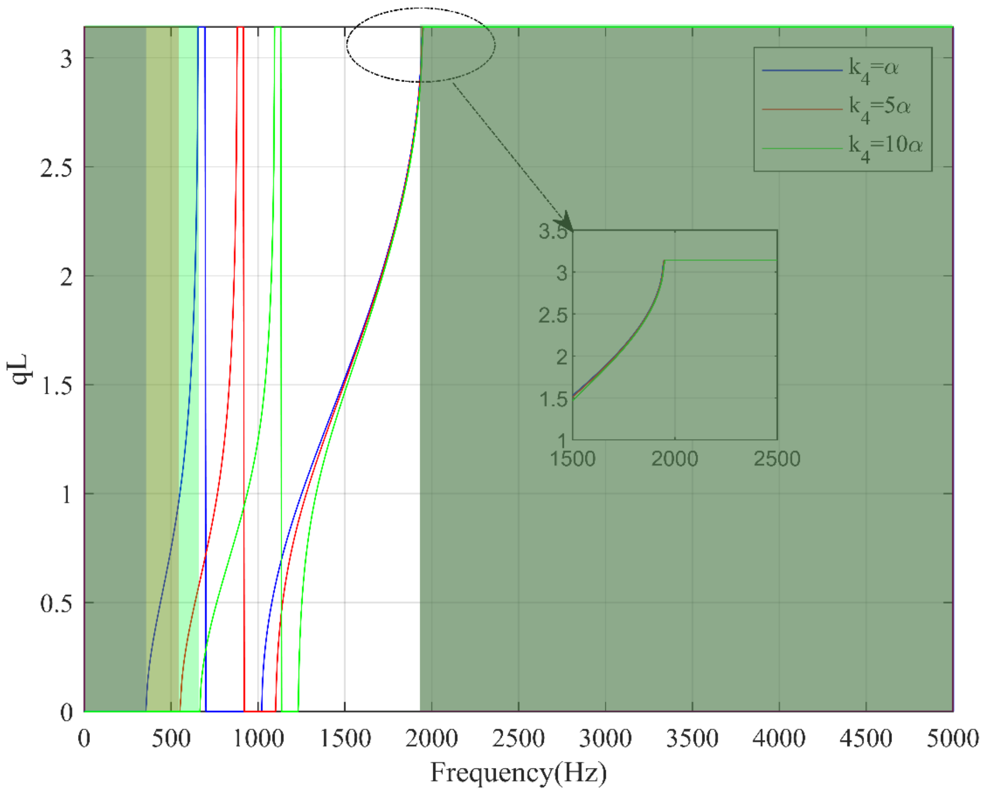

Fig. 10. Dispersion relations of meta-lattice truss embedded with the resonator with varied values of k_4.

Analogously, the effects of the parameters k_1, k_2, and k_3 on the bandgap behavior are examined and the results are shown in Table 5. It is clear that increasing the shear spring stiffness k_2 narrows the frequency region of the third bandgap, but results in a surge of the other two bandgaps. On the other hand, for the axial stiffness k_1 and k_3, while increasing the stiffness exerts no effect on the first bandgap, they narrows the third bandgap, and result an increase and stability on the second bandgap by increasing k_3 and k_1, respectively. In summary, the third bandgap associated with high frequencies is more sensitive to the stiffness k_1, k_2 and k_3, while the axial stiffness exhibits no influence on the first bandgaps. It is also noted that the sensitivity of the spring stiffness to the bandgaps can be qualitatively predicted using Eqs. (21) and (22), as mentioned previously.

Table 5. Meta-lattice truss characteristics with varied stiffness k_1, k_2, and k_3.

Stiffness	Value	1st Bandgap	2nd Bandgap	3rd Bandgap
k_2	α	0-375 Hz	700-1100 Hz	1945-5000 Hz
	5α	0-550 Hz	700-1250 Hz	2100-5000 Hz
	10α	0-620 Hz	700-1610 Hz	2305-5000 Hz
k_1	α	0-375 Hz	700-1100 Hz	1945-5000 Hz
	5α	0-375 Hz	700-1100 Hz	3500-5000 Hz
	10α	0-375 Hz	700-1100 Hz	3945-5000 Hz
k_3	α	0-375 Hz	700-1100 Hz	1945-5000 Hz
	5α	0-375 Hz	1400-2100 Hz	2700-5000 Hz
	10α	0-375 Hz	2000-2900 Hz	3305-5000 Hz

6. Transient response of meta-lattice truss based on numerical simulation

The above analytical derivation and solution are valid for the meta-lattice truss with some assumptions, i.e., infinite unit cells and harmonic wave solution. In practice, a meta-lattice truss is applied with a finite number of unit cells and may be subjected to dynamic loading such as impact and blast which possess a wide range of frequencies. Deriving an analytical solution for the structural response of such meta-lattice truss is not straightforward. To surmount this limitation of the analytical solution, a finite element model of the meta-lattice truss is built in LS-DYNA to investigate the stress wave propagation in the structure.

In this section, the transient response of the meta-lattice truss under harmonic excitation is further examined with two cases including a sweep excitation [1-5000] Hz in Section 6.1 and a dominant frequency at 500 Hz in Section 6.2. The excitation is in the form of $u(t) = 10^{-4}\sin(2\pi ft)$. The finite element model developed above is adopted again to carry out the analyses. The stress waves in the time domain at the far end are captured to demonstrate the extraordinary characteristics of the meta-lattice truss.

6.1 Transient response to sweep excitation

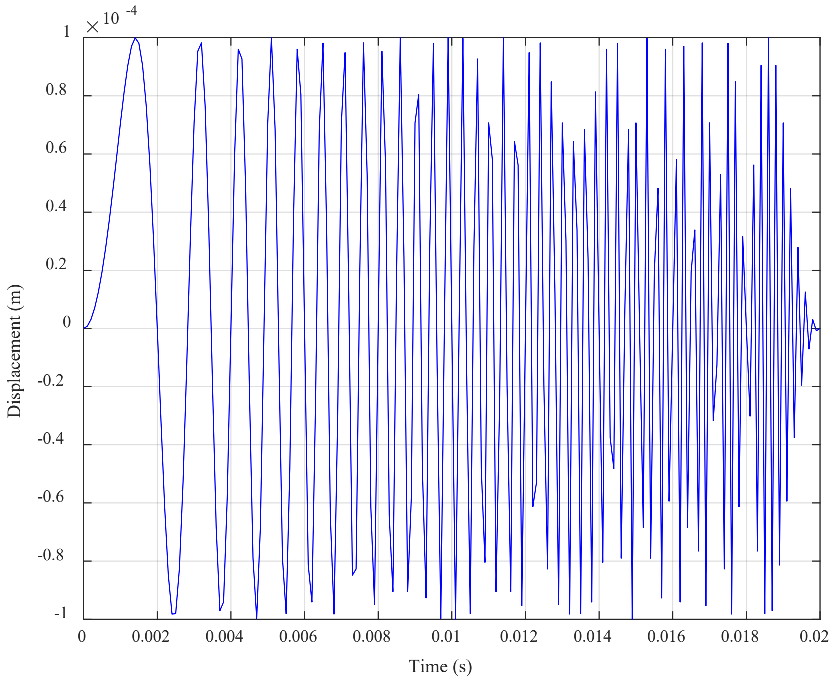

Fig. 11. Sweep excitation input profiles in time-domain.

Fig. 11 shows the sweep excitation at one end of the meta-lattice truss and Fig. 12 depicts the movement vector of each part of the entire structure at a typical instant. Fig. 12 (a) shows the displacement contour of each component of the 3D meta-lattice truss in which local resonators m_1 and m_2 do not have synchronized motions due to the local resonant mechanism that the hardcore acts as an oscillator. Specifically, the interaction of these two resonators (resonator 1 in white color and resonator 2 in yellow color) includes the in-phase motions (Fig. 12(b)) and the out-of-phase motions (Fig. 12(b)) working as energy absorbers can significantly mitigate the stress wave propagating through the structure.

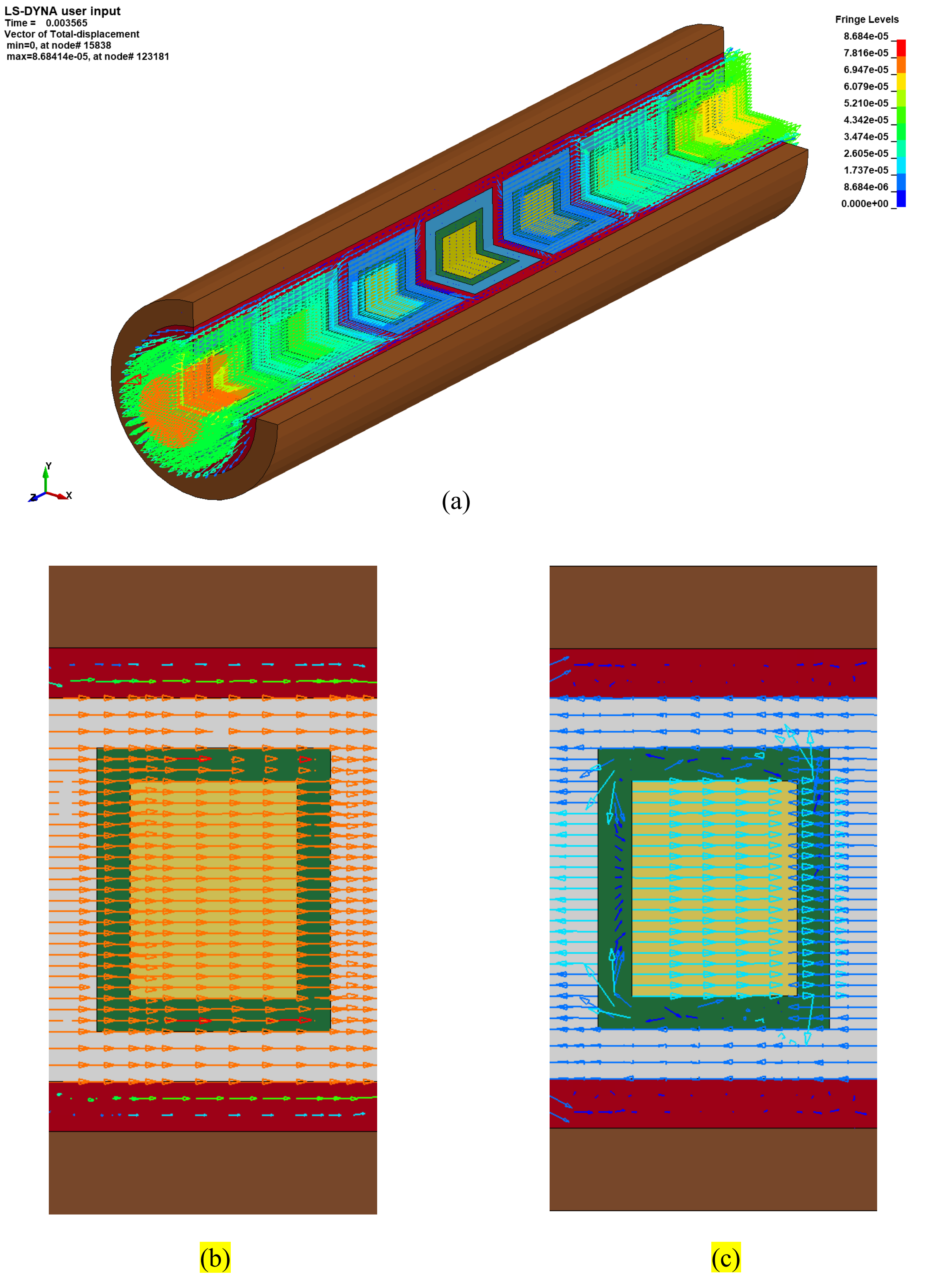

Fig. 12. Snapshots of the interaction displacement of the resonators (a) 3D Meta-lattice truss, (b) Cross section of unit 1 at t = 4.299 ms, and (c) Cross section of unit 1 at t = 6.449 ms.

To more explicitly show the wave attenuation effect, the Z-stress waves at different section of the outer mass aluminium (3rd layer in Fig. 1) and outer coating element (2nd layer in Fig. 1) are compared in Figs. 13(a) and 13(b), respectively. It can be seen that the amplitudes of the element close to the input excitation (input section in the figure) are largest while the smallest amplitudes belong to the element at the far-end position (the output section). The absolute maximum amplitudes of the stress waves at the three sections of the aluminum outer mass are $-1.4\text{x}10^6$, $-0.5\text{x}10^6$, $-0.3\text{x}10^6$ N/m^2, respectively, and the corresponding results in the external layer of rubber are $-1.7\text{x}10^6$, $-0.8\text{x}10^6$, $-0.4\text{x}10^6$ N/m^2. It is evident that both figures exhibit the stress wave attenuation from the beginning to the end of the meta-lattice truss subjected to the sweep frequency excitation.

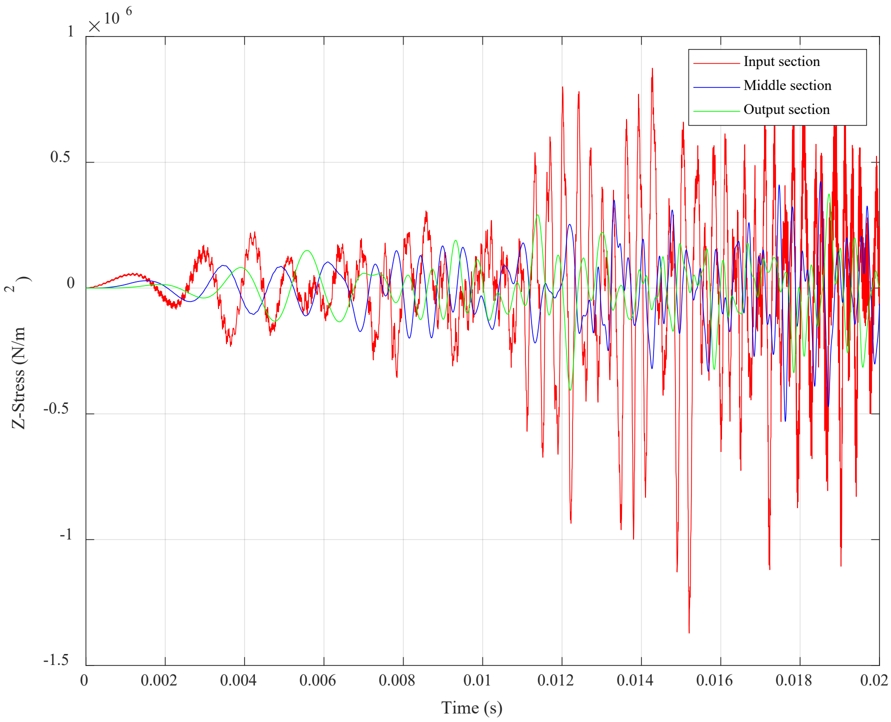

(a) Outer mass aluminium

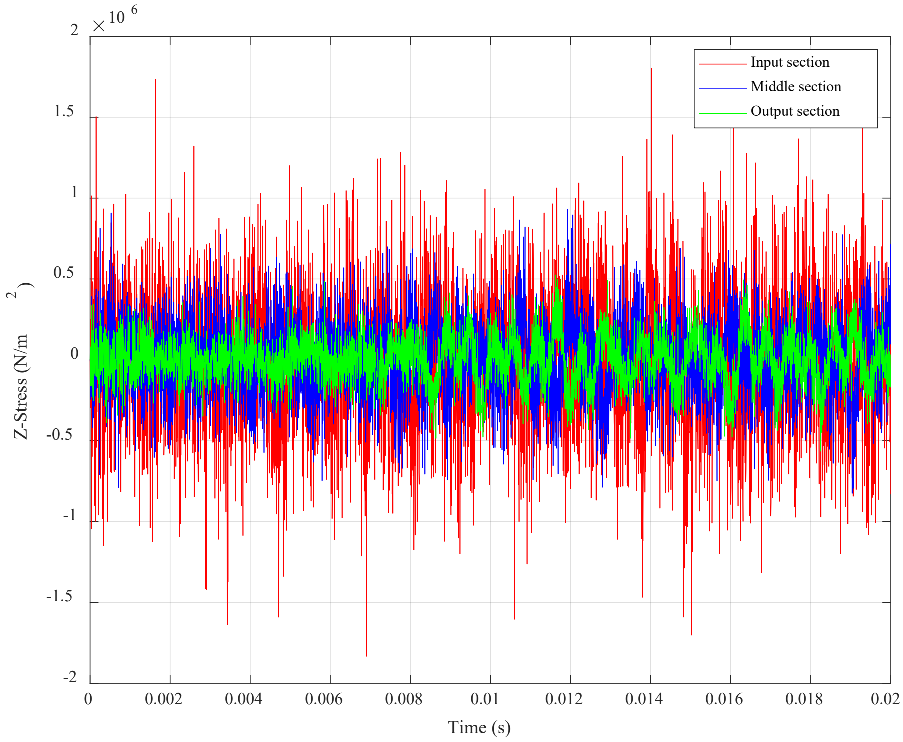

(b) Outer coating

Fig. 13. Stress waves time histories at different sections of the lattice truss subjected to excitation with sweep frequency ranging from 1-5000 Hz.

To further validate the proposed model, the continuous wavelet transform (CWT) is applied to analyze the output displacements in the time-frequency domain. In this study, a Gabor wavelet transform is chosen as the mother wavelet function owing to its multiresolution analysis capability. Figs. 14 depicts the multi-frequency CWT profiles of the far-end surface data in the case of sweep excitation. As shown, no energy exists in the output signal within three frequency ranges which are shaded in the figure, which mean the three bandgaps are formed. These bandgaps are well agreed with the analytical results as discussed above.

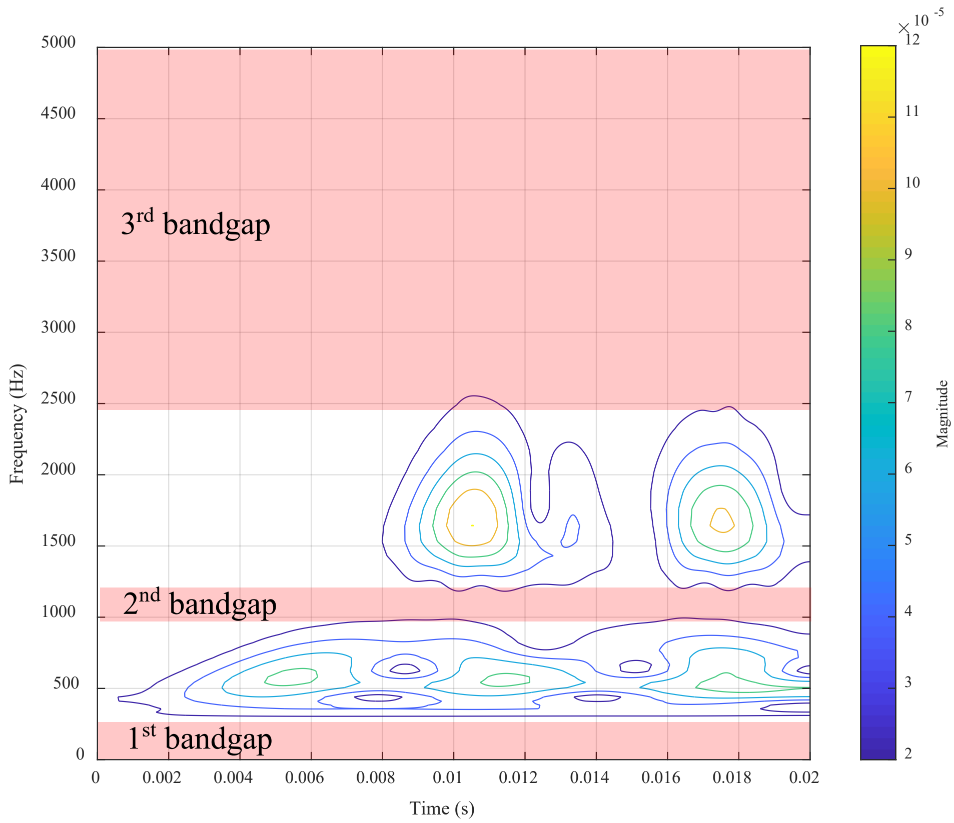

Fig. 14. Transient response profiles of the output displacement obtained by the CWT method in the time-frequency domain under the sweep excitation.

6.2 Transient response to a single frequency inside the passband

The dynamic response of the meta-lattice truss is further studied by applying a prescribed displacement with a frequency that falls outside the bandgap range. In the numerical simulation, a frequency of 500 Hz is chosen. By applying a similar procedure, the stress waves of an element in the lead core (5th layer in Fig. 1) and the inner coating (4th layer in Fig. 1) at the input end, middle part and output end of the model are compared in Figs. 15(a) and 15(b), respectively. It can be seen that no wave attenuation occurs because the wave frequency is outside the bandgap of the meta-lattice truss. In other words, the stress wave can propagate through the meta-lattice truss without any internal obstructions, there is no prominent change in the stress amplitude.

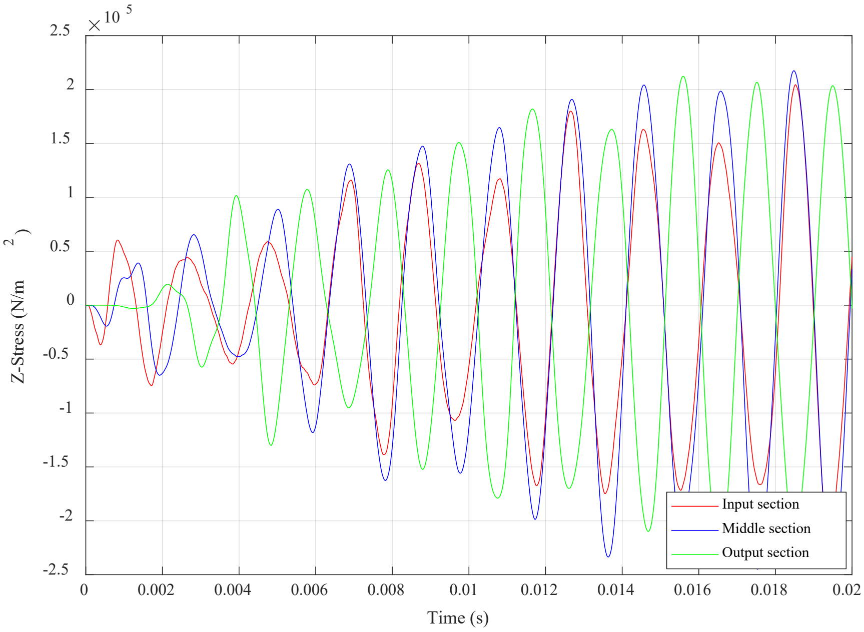

(a) Lead core

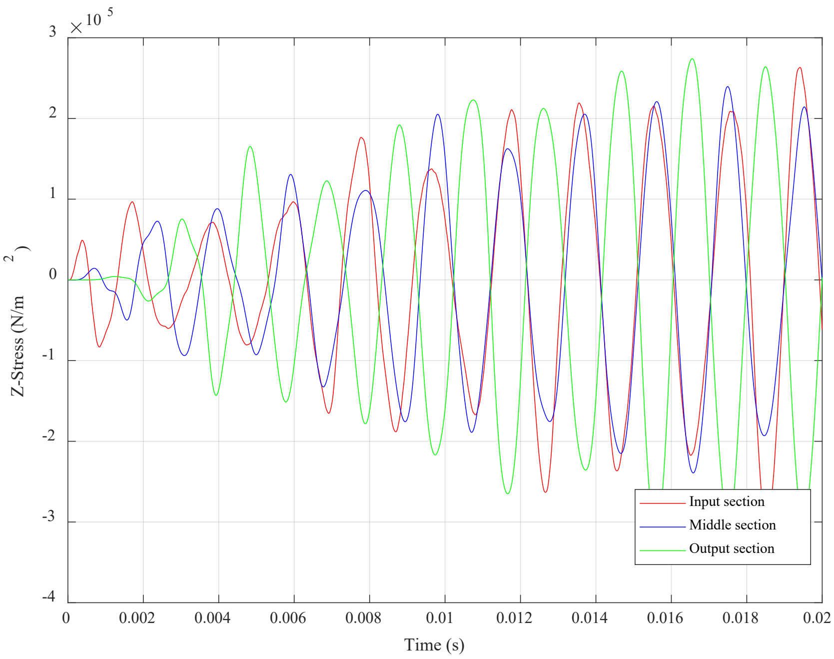

(b) Inner coating

Fig. 15. Stress waves time histories at different sections of the meta-lattice truss subjected to harmonic excitation with frequency out of the bandgap range.

Figs. 16 depicts the multi-frequency CWT profiles of the far-end surface subjected to a single frequency excitation (i.e. with the frequency of 500 Hz). As shown in Fig. 16, the dominant frequency of the transmitted signal remains unchanged at 500 Hz, which means no wave attenuation phenomena occurs in this area. This is because 500 Hz is within the passband of the meta-lattice truss as discussed above.

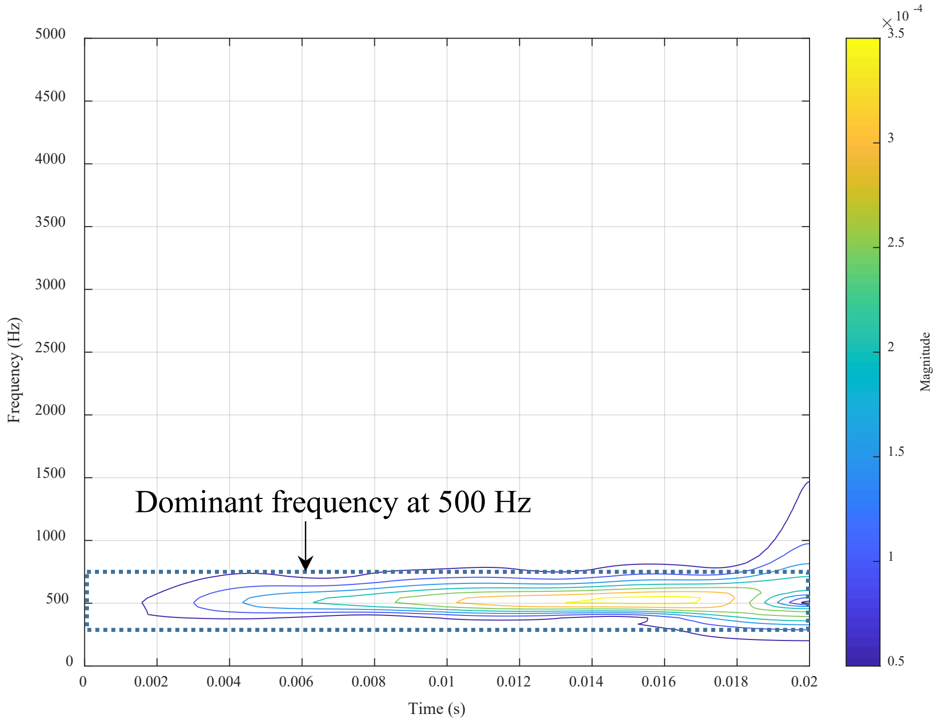

Fig. 16. Transient response profiles of the output displacement obtained by the CWT method in the time-frequency domain under the excitation with single frequency of 500 Hz.

7. Conclusions

In this study, an analytical mass-in-mass spring model is developed to improve the accuracy of the commonly used analytical model for the dynamic behaviors of the meta-lattice truss system. In the proposed model, one more spring representing the shear stiffness between the most inner core and the corresponding coating is taken into consideration. From the analytical and numerical investigations, the following conclusions can be drawn:

1. The proposed model results in a broader low-frequency bandgap for the meta-lattice truss, while this low-frequency bandgap width is under predicted by the conventional model owing to neglecting the shear stiffness of the second-layer coating connecting the inner and outer mass.

2. Parametric studies reveal that the first two bandgaps can be broadened by either increasing the internal mass m_1 or decreasing m_2 while the third bandgap remains unchanged irrespective of the value of m_2 but increases with m_1.

3. Increasing the axial stiffness k_1, and k_3 has no effect on the first bandgap but narrows the third bandgap. Increasing shear spring stiffness k_2 narrows the third bandgap, but widens the other two bandgaps. Increasing the shear stiffness k_4, which is neglected in the previous study, has no effect on the bandgap in the high-frequency range but widens the bandgap in the low-frequency range.

In general, the investigated meta-lattice truss with dual resonators exhibits excellent performance on stress wave mitigation so that it possesses a great potential to be deployed in protective structures or energy absorbers. The proposed analytical model can predict the performance of the meta-lattice truss with a high level of accuracy in the low-frequency range.

Acknowledgments

The authors would like to acknowledge the financial support from the Australian Research Council via Laureate Fellowships FL180100196 and the Research Training Program Scholarship (RTP) from Curtin University.

Appendix

With an attempt to estimate the accurate values of the spring stiffness k_i (i=1,2,3,4), the commercial software COMSOL MULTIPHYSICS was leveraged to conduct a numerical simulation. A constant force F which is depicted in Fig. 17(a) is applied to the model to calculate the value of shear spring stiffness k_4 of the internal core and while two constant force F was put in two directions of the model to estimate the values of k_3 shown in Fig. 18(a). Similarly, the calculation of value k_2 and k_1 is carried out with the same procedure but different dimensions. As seen in Fig. 17(a) and 18(a), the average displacements monitored at the yellow surface are denoted as u_i (i=1,2,3,4) and captured by commercial software which is observed in Fig. 17(b) and 18(b). The boundary condition for all edges of the outer shell is clamped. The equilibrium equations of the unit model are as follows [34]:

$$k_1(u_1+u_2)+k_2u_1=F \tag{30}$$

$$k_2u_3=F$$

$$k_3(u_4+u_5)+k_4u_4=F$$

$$k_4u_6=F$$

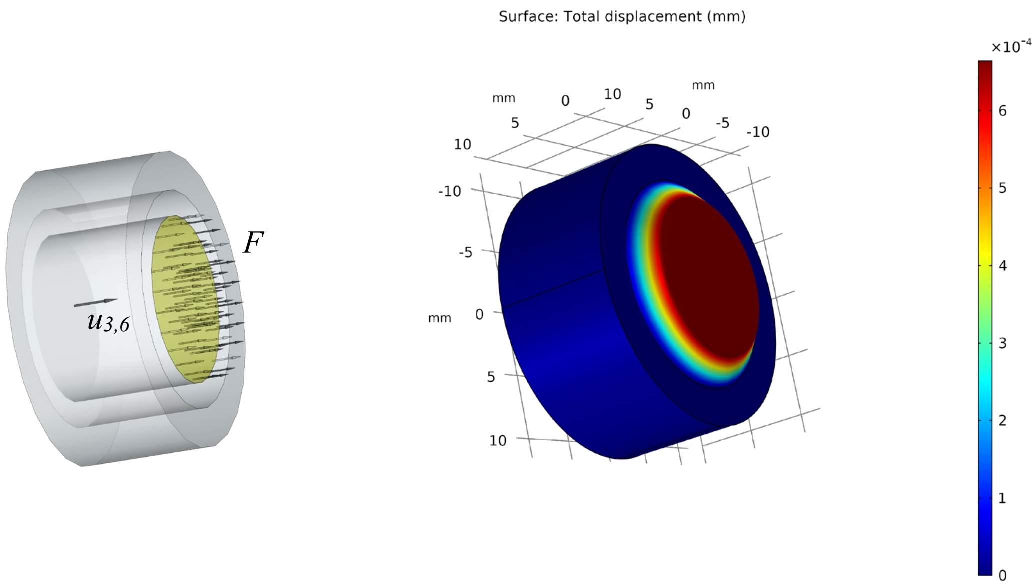

(a) (b)

Fig.17. Simulated model utilized for the calculation of k_2 and k_4 (a) Undeformed model (b) Deformed model.

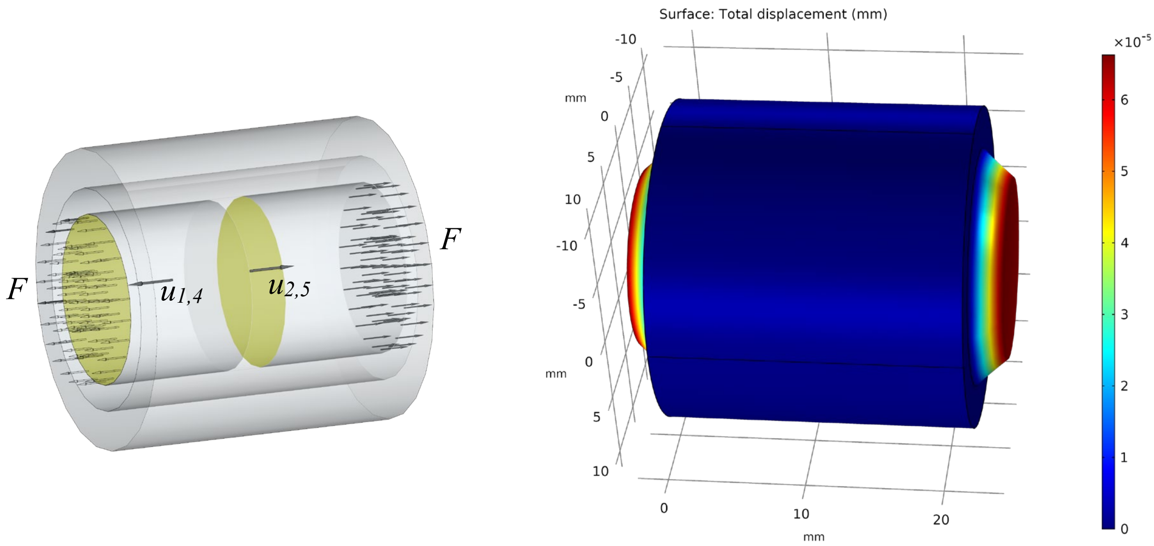

(a) (b)

Fig.18. Simulated model utilized for the calculation of k_1 and k_3 (a) Undeformed model (b) Deformed model.

The approximate value of the stiffness k_i (i=1,2,3,4) can be estimated by Young's modulus E and shear modulus G based on the relevant cross-sections of different parts of rubber A_i (i=1,2,3,4) which is presented in Figs. 19(a) and 19(b).

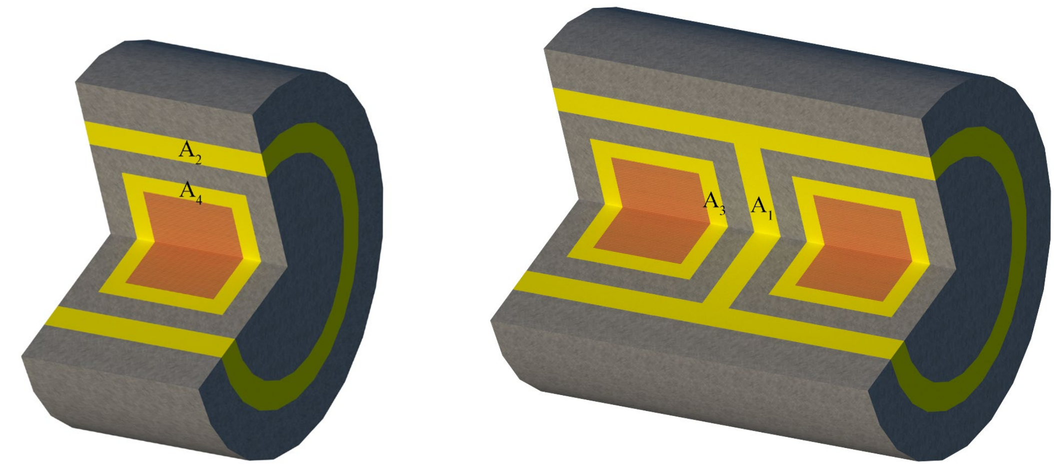

(a) (b)

Fig.19. Schematic diagram for the calculation of the cross-section value (a) A_2 and A_4 and (b) A_1 and A_3.

References

[1] D. Lee, D.M. Nguyen, J. Rho, Acoustic wave science realized by metamaterials, Nano Convergence, 4 (2017) 3.

[2] V.G. Veselago, The Electromanatics of Substances with Simultaneously Negative Value of e and μ, Soviet Physics Uspekhi, 10 (1968) 509-514.

[3] R.M. Walser, Electromagnetic metamaterials, SPIE, 2001.

[4] L. Fan, Z. Chen, S.-y. Zhang, J. Ding, X.-j. Li, H. Zhang, An acoustic metamaterial composed of multi-layer membrane-coated perforated plates for low-frequency sound insulation, Appl. Phys. Lett., 106 (2015) 151908.

[5] D. Powell, Core Concept: Mechanical metamaterials bend the rules of everyday physics, Proceedings of the National Academy of Sciences, 115 (2018) 2545.

[6] Y. Cheng, T. Yu, X. Zhou, Control of underwater acoustics using anisotropic solid metamaterials with continuously tuned material axes, Extreme Mechanics Letters, 32 (2019) 100544.

[7] H. Qin, D. Yang, C. Ren, Modelling theory of functional element design for metamaterials with arbitrary negative Poisson's ratio, Computational Materials Science, 150 (2018) 121-133.

[8] H. Wang, Y. Zhang, W. Lin, Q.-H. Qin, A novel two-dimensional mechanical metamaterial with negative Poisson’s ratio, Computational Materials Science, 171 (2020) 109232.

[9] J. Qu, M. Kadic, M. Wegener, Three-dimensional poroelastic metamaterials with extremely negative or positive effective static volume compressibility, Extreme Mechanics Letters, 22 (2018) 165-171.

[10] H.H. Huang, C.T. Sun, Wave attenuation mechanism in an acoustic metamaterial with negative effective mass density, New J. Phys., 11 (2009) 013003.

[11] W. Witarto, S.J. Wang, C.Y. Yang, X. Nie, Y.L. Mo, K.C. Chang, Y. Tang, R. Kassawara, Seismic isolation of small modular reactors using metamaterials, AIP Adv., 8 (2018) 045307.

[12] Y. Zeng, Y. Xu, H. Yang, M. Muzamil, R. Xu, K. Deng, P. Peng, Q. Du, A Matryoshka-like seismic metamaterial with wide band-gap characteristics, International Journal of Solids and Structures, 185-186 (2020) 334-341.

[13] Z. Lu, X. Yu, S.-K. Lau, B.C. Khoo, F. Cui, Membrane-type acoustic metamaterial with eccentric masses for broadband sound isolation, Appl. Acoust., 157 (2020) 107003.

[14] X. Xiang, X. Wu, X. Li, P. Wu, H. He, Q. Mu, S. Wang, Y. Huang, W. Wen, Ultra-open ventilated metamaterial absorbers for sound-silencing applications in environment with free air flows, Extreme Mechanics Letters, 39 (2020) 100786.

[15] X. An, C. Lai, H. Fan, C. Zhang, 3D acoustic metamaterial-based mechanical metalattice structures for low-frequency and broadband vibration attenuation, International Journal of Solids and Structures, 191-192 (2020) 293-306.

[16] P.F. Pai, H. Peng, S. Jiang, Acoustic metamaterial beams based on multi-frequency vibration absorbers, Int J Mech Sci, 79 (2014) 195-205.

[17] K.T. Tan, H.H. Huang, C.T. Sun, Blast-wave impact mitigation using negative effective mass density concept of elastic metamaterials, Int J Impact Eng, 64 (2014) 20-29.

[18] E. Kim, J. Yang, H. Hwang, C.W. Shul, Impact and blast mitigation using locally resonant woodpile metamaterials, Int J Impact Eng, 101 (2017) 24-31.

[19] M.H. Khan, B. Li, K.T. Tan, Impact load wave transmission in elastic metamaterials, Int J Impact Eng, 118 (2018) 50-59.

[20] A. Hall, E. Calius, G. Dodd, E. Wester, Modelling and experimental validation of complex locally resonant structures, 2019.

[21] A.O. Krushynska, V.G. Kouznetsova, M.G.D. Geers, Towards optimal design of locally resonant acoustic metamaterials, J. Mech. Phys. Solids., 71 (2014) 179-196.

[22] S. Ning, F. Yang, C. Luo, Z. Liu, Z. Zhuang, Low-frequency tunable locally resonant band gaps in acoustic metamaterials through large deformation, Extreme Mechanics Letters, 35 (2020) 100623.
[23] A. Madeo, P. Neff, I.-D. Ghiba, G. Rosi, Reflection and transmission of elastic waves in non-local band-gap metamaterials: A comprehensive study via the relaxed micromorphic model, J. Mech. Phys. Solids., 95 (2016) 441-479.
[24] I.L. Chang, Z.-X. Liang, H.-W. Kao, S.-H. Chang, C.-Y. Yang, The wave attenuation mechanism of the periodic local resonant metamaterial, J. Sound. Vib., 412 (2018) 349-359.
[25] M. Omelyanovich, V. Ovchinnikov, C. Simovski, A non-resonant dielectric metamaterial for the enhancement of thin-film solar cells, Journal of Optics, 17 (2015) 025102.
[26] C. Comi, L. Driemeier, Wave propagation in cellular locally resonant metamaterials, Lat. Am. J. Solid. Struct., 15 (2018).
[27] S. Cho, B. Kim, D. Min, J. Park, Tunable two-dimensional acoustic meta-structure composed of funnel-shaped unit cells with multi-band negative acoustic property, J. Appl. Phys., 118 (2015) 163103.
[28] B. Li, S. Alamri, K.T. Tan, A diatomic elastic metamaterial for tunable asymmetric wave transmission in multiple frequency bands, Sci. Rep., 7 (2017) 6226.
[29] Y. Chen, F. Qian, L. Zuo, F. Scarpa, L. Wang, Broadband and multiband vibration mitigation in lattice metamaterials with sinusoidally-shaped ligaments, Extreme Mechanics Letters, 17 (2017) 24-32.
[30] W. Milton, R. Willis, On modifications of Newton's second law and linear continuum elastodynamics, Proceedings of the Royal Society A: Mathematical, Physical and Engineering Sciences, 463 (2007) 855-880.
[31] Y. Liu, X. Su, C.T. Sun, Broadband elastic metamaterial with single negativity by mimicking lattice systems, J. Mech. Phys. Solids., 74 (2015) 158-174.
[32] Y. Liu, X. Shen, X. Su, C.T. Sun, Elastic Metamaterials With Low-Frequency Passbands Based on Lattice System With On-Site Potential, J. Vib. Acoust., 138 (2016) 021011-021011-021010.
[33] S. Alamri, B. Li, G. McHugh, N. Garafolo, K.T. Tan, Dissipative diatomic acoustic metamaterials for broadband asymmetric elastic-wave transmission, J. Sound. Vib., 451 (2019) 120-137.
[34] B. Li, Y. Liu, K.-T. Tan, A novel meta-lattice sandwich structure for dynamic load mitigation, J. Sandw. Struct. Mater., (2017) 1099636217727144.
[35] F. Farzbod, M. Leamy, Analysis of Bloch’s Method and the Propagation Technique in Periodic Structures, J. Vib. Acoust., 133 (2011) 031010.
[36] S. Yao, X. Zhou, G. Hu, Experimental study on negative effective mass in a 1D mass–spring system, New J. Phys., 10 (2008) 043020.
[37] P. Tran, S. Linforth, T.D. Ngo, R. Lumantarna, T.Q. Nguyen, Design analysis of hybrid composite anti-ram bollard subjected to impulsive loadings, Compos. Struct., 189 (2018) 598-613.
[38] L.-C. Alil, L.-C. Matache, S. Sandu, Numerical Simulation of a Ballistic Impact on Tensylon® UHMWPE Laminates Using the Plastic Kinematic Model in LS-Dyna®, Journal of Military Technology, 1 (2018) 43-50.

List of Figures

Fig. 19. Schematic diagram for the calculation of the cross-section value (a) A_2 and A_4 and (b) A_1 and A_3.

List of Tables